CHAPTER 7

Scaling-Up of Photoreactors: Applications to Advanced Oxidation Processes

Orlando M. Alfano* and **Alberto E. Cassano**

Contents

Sections 2, 3, and 4 of this Chapter correspond to contributions that have been written with the following coworkers: Horacio A. Irazoqui, Carlos A. Martín, Rodolfo J. Brandi, Cristina S. Zalazar, Marisol D. Labas, Gustavo E. Imoberdorf, and María L. Satuf.

INTEC (Universidad Nacional del Litoral and CONICET), 3000 Santa Fe, Argentina

* Corresponding author.
E-mail address: alfano@santafe-conicet.gov.ar

Advances in Chemical Engineering, Volume 36
ISSN 0065-2377, DOI: 10.1016/S0065-2377(09)00407-4

1. INTRODUCTION

The analysis and design of homogeneous or heterogeneous photochemical reactors is a particular case of a chemical reactor in which case the radiation contribution of the conservation energy principle has two special characteristics: (i) it will always be present regardless of the operating temperature and (ii) since the majority of these reactions are carried out at a fixed, close to room temperature, and, usually, maintained under isothermal conditions, the radiation contribution can be uncoupled from the thermal energy equation. With this consideration, the modeling of the reactor based on first principles requires as usual, the solution of the momentum, thermal energy, and multicomponent mass conservation equations adding, in a photoreactor, the radiation energy contribution, in terms of a photon balance. However, it must be taken into account along the design, that the main objectives of its inclusion are the resulting kinetics effects derived by its dominant participation in initiating the reaction.

It is rather atypical that a photochemical reaction will proceed in a single molecular pathway. Thus, several elementary steps are involved. Normally, the majority of them are dark (thermal) reactions while, ordinarily, one activation step is produced by radiation absorption by a reactant molecule or a catalyst. From the kinetics point of view, dark reactions do not require a different methodological approach than conventional thermal or thermal-catalytic reactions. Conversely, the activation step constitutes the main distinctive aspect between thermal and radiation activated reactions. The rate of the radiation activated step is proportional to the absorbed, useful energy through a property that has been defined as the local volumetric rate of photon absorption, LVRPA (Cassano et al., 1995; Irazoqui et al., 1976) or the local superficial rate of photon absorption, LSRPA (Imoberdorf et al., 2005). The LVRPA represents the amount of photons that are absorbed per unit time and unit reaction volume and the LSRPA the amount of photons that are absorbed per unit time and unit reaction surface. The LVRPA is a property that must be used when radiation absorption strictly occurs in a well-defined three-dimensional (volumetrical) space. On the other hand, to

treat wall-catalyzed photochemical reactions of superficial nature, the LSRPA is the most apt property to treat this special physical configuration.

The concept of absorbed useful energy is very important to avoid the frequent confusion of considering the radiation source output energy as equivalent to the useful absorbed photons. The second comprises the consideration of all the physical processes that are involved from the moment and place that a photon leaves the lamp boundaries to the time and position in which the photon is finally taken up by the radiation absorbing species.

The methodology to treat the activation step is much better understood if one resort to the typical approach used in chemical reaction engineering. Figure 1 illustrates the concept. Starting from the necessary first step, one writes a mass balance. Either in the differential equation or in its boundary conditions the reaction rate for each participating species must be formulated. When the expression for the reaction rate of the species under consideration involves the activation step, it necessarily involves the photon absorption rate (either volumetric or superficial). Its evaluation is performed stating first the radiative transfer equation (RTE) that requires the appropriate constitutive equations for radiation absorption, emission, scattering and seldom internal spontaneous or induced emission (Ozisik, 1973). In the most general case, the RTE is an integro-differential equation that involves all the constitutive equations for the comprised physical phenomena previously mentioned as well as the appropriate boundary conditions. For participating media, the constitutive equations invariably involve physical properties that depend of each particular case: absorption and scattering coefficients as well as the scattering phase function. Differently, absorption and

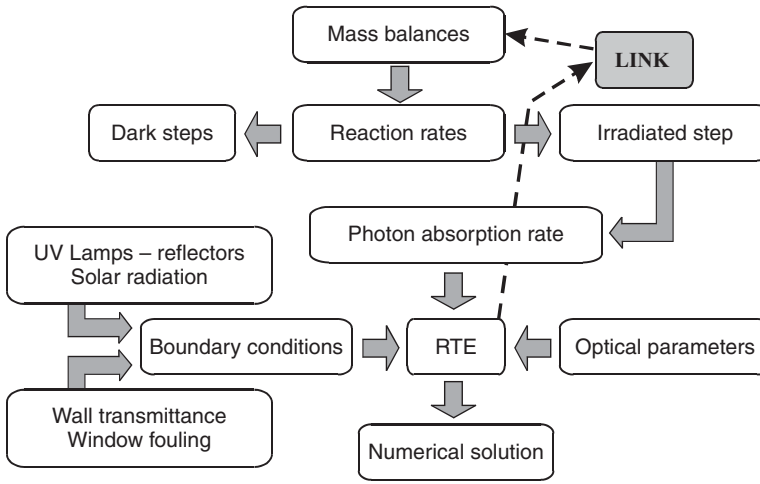

Figure 1 Evaluation of the photon absorption rate.

refection coefficients are needed for nonparticipating media. In its turn, the boundary conditions for the RTE must account for the existence of UV lamps and reflectors (or direct and diffuse radiation for solar reactors) as well as the effects of the reactor walls (for example, wall transmittance, including reflections and refractions, and sometimes, fouling of the radiation entrance window). The result is a completely defined RTE that will be applied to each reactor configuration. In the detailed description of the method in this chapter, the resulting RTE will be successively applied to a reaction space for a nonparticipating medium (Section 2), a homogeneous medium where there is only radiation absorption (Section 3), and a heterogeneous medium where radiation absorption and scattering are present (Section 4).

A very important point to emphasize is that the RTE is written considering two important aspects of the radiation propagation: (i) the direction of flight (movement in space) of the radiation beam and (ii) the energy transported by the photon traveling in such direction. Thus, the RTE is derived for a single propagating direction and a single wavelength. This is better realized resorting to the graphical illustration presented by Alfano and Cassano (2008). Figure 2a shows a photon distribution in directions and wavelengths (or frequencies) in an elementary volume V in space, bounded by a surface A having an outwardly directed normal $\underline{n}$. This figure illustrates the case of photons with indiscriminate directions and different wavelengths in the mentioned elementary volume. For example, white dots can represent a wavelength λ_n and black dots a wavelength λ_m. Then, in Figure 2b, photons with any direction and having a single wavelength (white dots or λ_n) are exemplified. Finally, Figure 2c illustrates photons having a single direction and a single wavelength (λ_n).

This visual conception helps to define the fundamental property for characterizing the radiation field in a photochemical reactor: the spectral

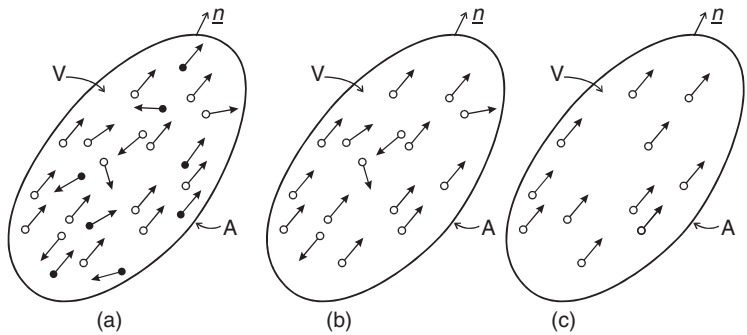

Figure 2 Characterization of the photon distribution in directions and wavelengths.

specific intensity. This radiation property is defined as the amount of energy per unit time, per unit normal area, per unit solid angle, and per unit wavelength interval:

$$I_{\underline{\Omega}\lambda}(\underline{x},t) = \lim_{(\Delta S,\Delta\Omega,\Delta t,\Delta\lambda)\to 0}\left(\frac{\Delta E_\lambda}{\Delta A\,\cos\theta\,\Delta\Omega\,\Delta t\,\Delta\lambda}\right) \tag{1}$$

having units of Einstein s^{-1} m^{-2} sr^{-1} m^{-1} (or nm^{-1}). Note that the monochromatic (λ) radiation intensity is a function of position ($\underline{x}$), direction ($\underline{\Omega}$), and time (t). This means that its complete definition involves three spatial coordinates, two directional coordinates (usually in a spherical coordinate system), and a temporal coordinate. The property that is used to formulate the RTE is the starting point to calculate the Incident Radiation at any material point inside a reaction space or the Radiation Flux Density for wall-catalyzed photochemical reactions.

Employing the spectral specific intensity, it is then possible to write a photon balance in a bounded volume as follows (Cassano et al., 1995; Ozisik, 1973):

Time rate of change of $(\lambda,\underline{\Omega})$ photons in the volume V	+	Net flux of $(\lambda,\underline{\Omega})$ photons leaving the volume V across the surface A	=	Net gain of $(\lambda,\underline{\Omega})$ photons owing to emission, absorption, in- and out-scattering in the volume V

Considering the two source terms (emission and in-scattering) and the two sink terms (absorption and out-scattering) defined on the right-hand side of the previous expression, one can transform the preceding fundamental law in a more formal mathematical definition:

$$\frac{1}{c}\frac{\partial I_{\lambda,\underline{\Omega}}}{\partial t} + \underline{\nabla}\cdot(I_{\lambda,\underline{\Omega}}) = W^{\text{em.}}_{\lambda,\underline{\Omega}} - W^{\text{abs.}}_{\lambda,\underline{\Omega}} - W^{\text{out-scatt.}}_{\lambda,\underline{\Omega}} + W^{\text{in-scatt.}}_{\lambda,\underline{\Omega}} \tag{2}$$

It is now possible to introduce two simplifications rationalized as follows: (i) since the selected applications will be usually operated at room temperatures, internal emission can be safely neglected ($W^{\text{em.}}_{\lambda,\underline{\Omega}} = 0$) and (ii) considering the magnitude of the light speed c, the first term is unequivocally neglected in all practical cases ($1/c)(\partial I_{\lambda,\underline{\Omega}}/\partial t) \cong 0$.

As written, Equation (2) is the general formulation of a radiation balance for a single direction and a given amount of transported energy, but it is not very useful because we do not have sufficient information to evaluate the terms in its right-hand side. With the same approximation rigorously employed in continuous mechanics, the problem is solved with the introduction of a constitutive equation for each term, resorting to the

measurement of the discernible behavior of each phenomenon and its relationship with the involved observable physical properties affecting each one of the listed events. With this consideration, the RTE takes the following form:

$$\frac{\mathrm{d}I_{\underline{\Omega},\lambda}}{\mathrm{d}s}(s,t) + \underbrace{\kappa_\lambda(s,t) I_{\underline{\Omega},\lambda}(s,t)}_{\text{Absorption}} + \underbrace{\sigma_\lambda(s,t)\, I_{\underline{\Omega},\lambda}(s,t)}_{\text{Out-scattering}} = \underbrace{\frac{\sigma_\lambda(s,t)}{4\pi} \int_{\Omega'=4\pi} p_\lambda(\underline{\Omega}' \to \underline{\Omega})\, I_{\underline{\Omega},\lambda}(s,t)\, \mathrm{d}\Omega'}_{\text{In-scattering}} \tag{3}$$

A significant part of the potential applications of photoreactors are related with their capacity to be used in different processes of air, water, and soil remediation and are recognized with the generic name of advanced oxidation technologies. They are characterized in the majority of the cases by resorting to reactions that produce hydroxyl radicals as the main oxidant agent. These practices will be used to illustrate the proposed scaling-up procedures.

The general methodology for all applications is the same. One must model precisely the laboratory reactor even if it is very small with almost the same tools that are used in the larger scale. Figure 3, depicts the different steps of the method. Advancing to the change of scale, the kinetic model for the reaction obtained in the laboratory experiments (and the same catalyst when corresponds) must be used. This introduces the strict requirement that the obtained kinetics must be a point value function, valid for any reactor shape and/or arrangement. It can be seen that in the above assertion there is an obvious exception: the photon absorption rate in the kinetic expression must be calculated from a different radiation balance derived for the particular geometry of the larger reactor. For this reason, it should not be unexpected that in changing scales the mass and radiation balances will almost always be very different, because they are very dependent on the new proposed, reactor size, shape, configuration, and operation. In what follows, it will be also shown that both the laboratory reactor and the large-scale reactor must be strictly using the same wavelength spectral distribution of the employed input power.

2. SCALING-UP OF A PHOTOCATALYTIC WALL REACTOR WITH RADIATION ABSORPTION AND REFLECTION

The degradation of PCE in an air stream with different degrees of relative humidity was used in this first example. It was performed in a multitubular reactor of annular cross section (Imoberdorf et al., 2007). However, the design of this reactor is the last operation in the procedure illustrated by Figure 3.

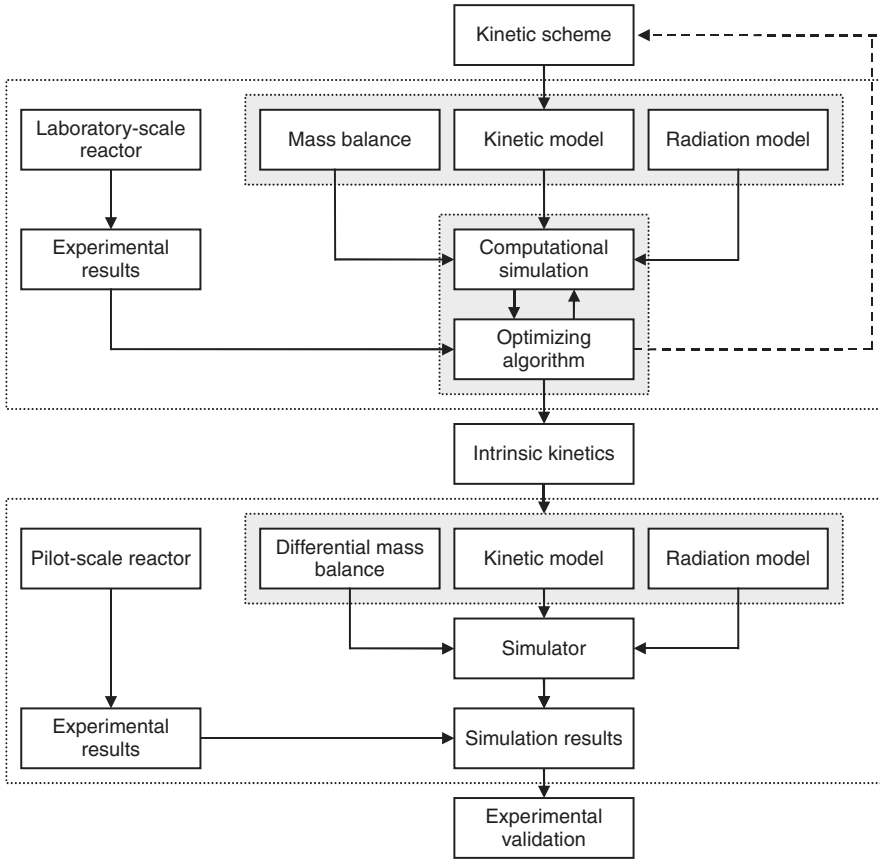

Figure 3 Scaling-up methodology.

2.1. Reaction scheme and kinetic model

The design of any form of photoreactor is greatly facilitated if a complete reaction sequence (even better if it is a true reaction mechanism) is known. On the basis of previous work, particularly the one reported by Yamazaqui and Araki (2002), the kinetic mechanism described in Table 1, was adopted. However, a complete reaction model and its kinetic parameters are needed. This is the first important step in the method.

To derive the kinetic model from the reaction scheme, the following assumptions were made: (i) the formation of OH• in steps 2 and 3 can be grouped in a single kinetic constant, (ii) the PCE degradation occurs through an elementary reaction involving the PCE attack by OH• radicals followed by a sequence of steps that leads to the generation of a chlorine atom and a chain reaction initiated by the attack of the Cl• on the PCE,

Table 1 Proposed kinetic scheme for the PCE degradation

Radiation activation	$TiO_2 \rightarrow TiO_2 + e^- + h^+$	R_g
OH• generation	$h^+ + H_2O_{ads} \rightarrow OH\cdot + H^+$ $h^+ + HO^-{}_{ads} \rightarrow OH\cdot$	$\left\{k_1\right.$
	$e^- + O_2 \rightarrow O_2^-\cdot$	k_2
Cl• generation	$C_2Cl_{4\ ads} + OH\cdot \rightarrow C_2Cl_4OH\cdot$	k_3
	$C_2Cl_4OH\cdot + O_2 \rightarrow C_2Cl_4OHOO\cdot$	k_4
	$2C_2Cl_4OHOO \rightarrow 2C_2Cl_4OHO\cdot + O_2$	k_5
	$C_2Cl_4OHO\cdot \rightarrow C_2Cl_3OHO + Cl\cdot$	k_6
Chain propagation	$C_2Cl_{4ads} + Cl\cdot \rightarrow C_2Cl_5\cdot$	k_7
	$C_2Cl_5\cdot + O_2 \rightarrow C_2Cl_5OO\cdot$	k_8
	$2C_2Cl_5OO\cdot \rightarrow 2C_2Cl_5O\cdot + O_2$	k_9
	$C_2Cl_5O\cdot \rightarrow CCl_2O + CCl_3\cdot$	k_{10}
	$C_2Cl_5O\cdot \rightarrow C_2Cl_4O + Cl\cdot$	k_{11}
	$CCl_3\cdot + O_2 \rightarrow CCl_3OO\cdot$	k_{12}
	$2CCl_3OO\cdot \rightarrow 2CCl_3O\cdot + O_2$	k_{13}
	$CCl_3O\cdot \rightarrow CCl_2O + Cl\cdot$	k_{14}
Termination reactions	$e^- + h^+ \rightarrow$ heat	k_{15}
	$Cl\cdot + M \rightarrow$ products	k_{16}
Phosgene hydrolysis (fast)	$CCl_2O + H_2O \rightarrow CO_2 + 2HCl$	k_{17}
Adsorption	$C_2Cl_4 + Sites \leftrightarrow C_2Cl_{4ads}$	K_{PCE}
	$H_2O + Sites \leftrightarrow H_2O_{ads}$	K_W

Adapted from Imoberdorf et al. (2005).

(iii) the PCE decomposition in the first step of the chain propagation is much faster than that involving the direct attack by OH• and this result is translated into the degradation rate, (iv) the net generation rate of free radicals, atomic species, free electrons, and holes is null, (v) the termination reactions of atomic Cl• can be grouped in a single reaction between chlorine atoms and water vapor, other radical and atomic species, reactor walls and other surfaces in the system, and (vi) surface concentrations of adsorbed PCE and water can be related to the gas phase concentrations through adsorption equilibrium constants. All these assumptions have shown to be good approximations in the abundant literature concerning TCE degradation mentioned by Imoberdorf et al. (2005). Assuming that the kinetic information will be obtained in the absence of mass transfer limitations, with these approximations, the following expression was obtained:

$$\mathsf{R}_{\mathrm{PCE}} = -\frac{\alpha_1[\mathrm{PCE}]_{\mathrm{gas}}[\mathrm{H_2O}]_{\mathrm{gas}}}{\left(1+K_{\mathrm{PCE}}[\mathrm{PCE}]_{\mathrm{gas}}+K_W[\mathrm{H_2O}]_{\mathrm{gas}}\right)^2} \times\left(-1+\sqrt{\frac{1+K_{\mathrm{PCE}}[\mathrm{PCE}]_{\mathrm{gas}}+K_W[\mathrm{H_2O}]_{\mathrm{gas}}}{[\mathrm{H_2O}]_{\mathrm{gas}}}\alpha_2\mathsf{R}_g(\underline{x})+1}\right) \tag{4}$$

where the kinetic parameters α_1 and α_2 were defined by

$$\alpha_1=\frac{k_1k_2k_7K_{\mathrm{PCE}}K_W[\mathrm{Sites}]^2[\mathrm{O_2}]}{2k_{15}k_{16}[\mathrm{M}]} \text{ and } \alpha_2=\frac{4k_{15}}{k_1k_2K_W[\mathrm{Sites}][\mathrm{O_2}]} \tag{5}$$

The individual specific rate and adsorption equilibrium constants are defined in Table 1. In Equations (4) and (5) [Sites]refer to the available concentration of sites for adsorption on the TiO_2 film, $[O_2]$ to the liquid phase oxygen concentration, [M] to the concentration of water, atomic or free radical species, reactor walls or other surfaces trapping atomic chlorine, and R_g to the superficial rate of electrons and holes generation.

The local superficial rate of electron–hole pair generation can be computed considering a wavelength averaged primary quantum yield for the generation of charge carriers on the catalytic surface $\bar{\Phi}$:

$$\mathsf{R}_g(x)=\bar{\Phi}\sum_{\lambda}e_{\lambda}^{a,s}(\underline{\mathrm{x}})=\bar{\Phi}e^{a,s}(\underline{\mathrm{x}}) \tag{6}$$

The adopted average is needed because it is very difficult to obtain monochromatic primary quantum values. $e_{\lambda}^{a,s}(\underline{\mathrm{x}})$ is the spectral LSRPA on the surface of the catalytic wall. Substituting Equation (6) into Equation (4) gives

$$\mathsf{R}_{\mathrm{PCE}}(\underline{\mathrm{x}},t) = -\frac{\alpha_1[\mathrm{PCE}]_{\mathrm{gas}}[\mathrm{H_2O}]_{\mathrm{gas}}}{\left(1+K_{\mathrm{PCE}}[\mathrm{PCE}]_{\mathrm{gas}}+K_W[\mathrm{H_2O}]_{\mathrm{gas}}\right)^2} +\left(-1+\sqrt{\frac{1+K_{\mathrm{PCE}}[\mathrm{PCE}]_{\mathrm{gas}}+K_W[\mathrm{H_2O}]_{\mathrm{gas}}}{[\mathrm{H_2O}]_{\mathrm{gas}}}\alpha_2\bar{\Phi}e^{a,s}(\underline{\mathrm{x}})+1}\right) \tag{7}$$

From a plausible reaction sequence in Table 1 and reliable approximations, a local expression for the reaction kinetics in terms of observable and independent variables has been obtained. α_1 and α_2 are lumped kinetic parameters.

2.2. Laboratory reactor: description and modeling

The kinetics must be obtained in a reactor that should be as simple as possible with a well-characterized geometry in such a way that the obtained parameters are point value results of position and time. The laboratory device shown in Figures 4 and 5 is a continuous flow, well-mixed, recirculating reactor. The details are described in Table 2. The reader interested in

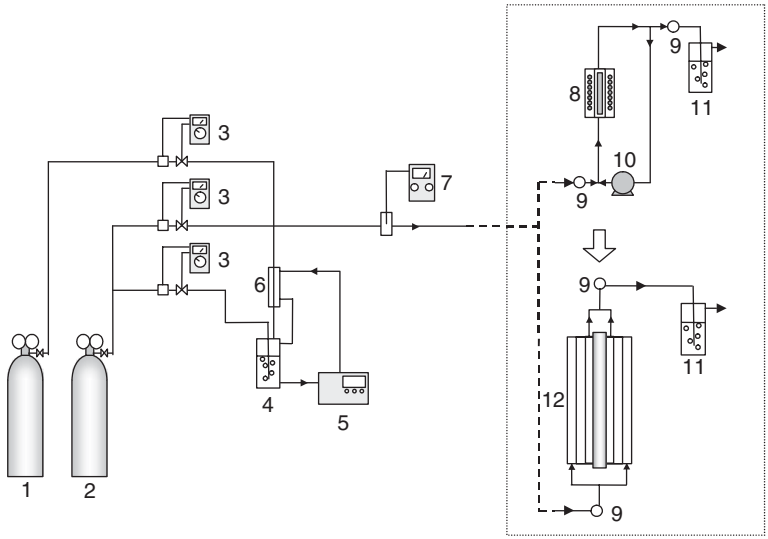

Figure 4 Laboratory and pilot scale photocatalytic reactors. Keys: (1) PCE + air, (2) air, (3) mass flowmeter, (4) air humidifier, (5) thermostatic bath, (6) heat exchanger, (7) thermohygrometer, (8) flat plate photoreactor, (9) sampling device, (10) recycle pump, (11) gas scrubber, (12) multiannular photocatalytic reactor.

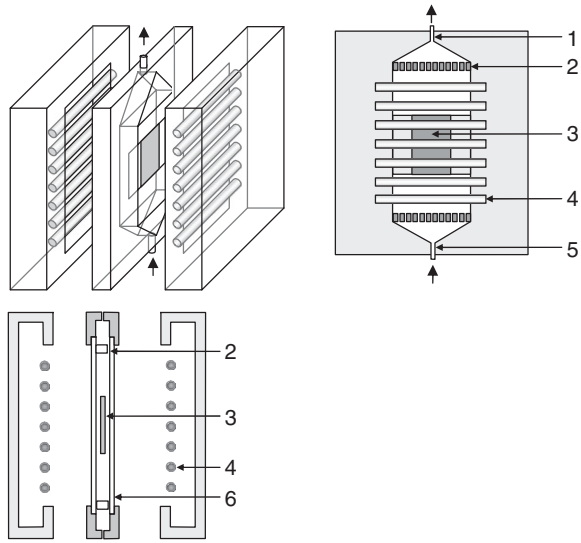

Figure 5 Schematic representation of the laboratory photoreactor. Keys: (1) gas outlet, (2) flow homogenizer, (3) photocatalytic plate, (4) UV lamps, (5) gas inlet, (6) acrylic windows.

Table 2 Laboratory and pilot scale reactor description and operating conditions

Item	Specification/Dimensions	
	Laboratory reactor	Pilot scale reactor
Type	Catalytic wall flat plate	Catalytic wall. Annular. Three concentric cylinders
Total surface	81 cm^2	5,209 cm^2
Dimensions	Two sides. Each: $x = 4.5\,cm^2 \times z = 9\,cm$	$Z_R = 48\,cm$, $R_{R,int} = 1.48\,cm$, $R_{R,ext} = 4.26\,cm$
Annulus I		$\chi_1 R_1 = 1.69\,cm,\ R_1 = 2.31\,cm$
Annulus II		$\chi_2 R_2 = 2.51\,cm,\ R_2 = 3.30\,cm$
Annulus III		$\chi_3 R_3 = 3.53\,cm,\ R_3 = 3.94\,cm$
Lamps	Seven in each side Philips TL 4W/08 F4T5/BLB Output power: 0.5 W each $\Delta\lambda = 300–420\,nm$ $Z_L = 13.6\,cm$, $R_L = 0.8\,cm$	One Philips TL 18W/08 F4TS/BLB Out put power: 3.5 W $\Delta\lambda = 300–420\,nm$ $Z_L = 59\,cm$, $R_L = 1.4\,cm$
Catalyst		
TiO_2	Sol-gel deposition	Sol-gel deposition
Operation		
Continuous	With recirculation: 2,000 $cm^3\ min^{-1}$	
Feed flow rate	20–200 $cm^3\ min^{-1}$	120–1,800 $cm^3\ min^{-1}$

Table 2 (*Continued*)

	Specification/Dimensions	
	Laboratory reactor	Pilot scale reactor
Temperature	20°C	20°C
Pressure	1 atm.	1 atm.
Inlet PCE concentration	10–30 mg m^{-3}	50 mg m^{-3}
Relative humidity	10–100%	10–90%
Irradiation level	Local net radiation flux on the reacting surface: $q = 4 \times 10^{-3}$ W cm^{-2}(100%)	LSRPA ($e^{a,s}$): From 1.6×10^{-9} to 1×10^{-11} Einstein cm^{-2} s^{-1}
Variation	(24–100%)	

Adapted from Imoberdorf et al. (2005, 2006, 2007).

more experimental information such as catalyst preparation, analytical procedures, start-up method, reaction times, conditions to exclude mass transfer limitations, and so on, can resort to the original work (Imoberdorf et al., 2005).

The mass conservation equation is very simple:

$$\langle \mathsf{R}_{\mathrm{PCE}} \rangle_{A_R} = \frac{Q^{\mathrm{in}} \left(\langle C_{\mathrm{PCE}} \rangle^{\mathrm{out}} - \langle C_{\mathrm{PCE}} \rangle^{\mathrm{in}} \right)}{A_R} \tag{8}$$

Considering the possibility of nonuniform coating (not occurring here) and nonuniform irradiation, the results are expressed in terms of an average value:

$$\langle \mathsf{R}_{\mathrm{PCE}} \rangle_{A_R} = \frac{1}{A_R} \int_{x=0}^{x=Xr} \int_{z=0}^{z=Zr} \mathsf{R}_{\mathrm{PCE}}(x,z) \mathrm{d}z\mathrm{d}x \tag{9}$$

It is clear that a model for the radiation field is required. It should be taken into account that PCE does not absorb radiation in the wavelength range of the employed radiation sources. Thus, the space surrounding the catalytic walls is not participative. According to Figure 6, the absorbed radiation must be calculated according to

$$e_{\lambda}^{a,s}(x,z) = (q_{\mathrm{dir},\lambda}^{i} - q_{\mathrm{dir},\lambda}^{t}) + (q_{\mathrm{ind},\lambda}^{i} - q_{\mathrm{ind},\lambda}^{t}) \tag{10}$$

where

$$q_{\lambda}(x,z) = \underline{\mathrm{n}}_g \cdot \underline{\mathrm{q}}_{\lambda} = \int_{\Omega_L} I_{\lambda}(x,y,\underline{\Omega})\underline{\Omega} \cdot \underline{n}_g \mathrm{d}\Omega \tag{11}$$

To solve Equation (11) one can resort to the three-dimensional source with superficial emission model (Cassano et al., 1995) and the ray tracing technique (Siegel and Howell, 2002). The integration limits depend on the geometry and dimensions of the reacting system and the set of the 14 employed lamps (Figures 5 and 6).

$$q_{\lambda}(r,z) = \sum_{i=1}^{n} \int_{\phi_{\min,L_i}}^{\phi_{\max,L_i}} \int_{\theta_{\min,L_i}(\phi)}^{\theta_{\max,L_i}(\phi)} I_{\lambda}(x,y,\phi,\theta) \sin^2\theta \sin\phi \, \mathrm{d}\theta\mathrm{d}\phi \tag{12}$$

The boundary conditions result

$$I_{\lambda}(r,z,\phi,\theta) = \begin{cases} 0 & (\phi,\theta) < (\phi_{\min,i},\theta_{\min,i}) \\ I_{\lambda,L} & = \dfrac{P_{\lambda,L}}{2\pi^2 R_L Z_L} (\phi_{\min,i},\theta_{\min,i}) < (\phi,\theta) < (\phi_{\max,i},\theta_{\max,i}) \\ 0 & (\phi_{\max,i},\theta_{\max,i}) < (\phi,\theta) \end{cases} \tag{13}$$

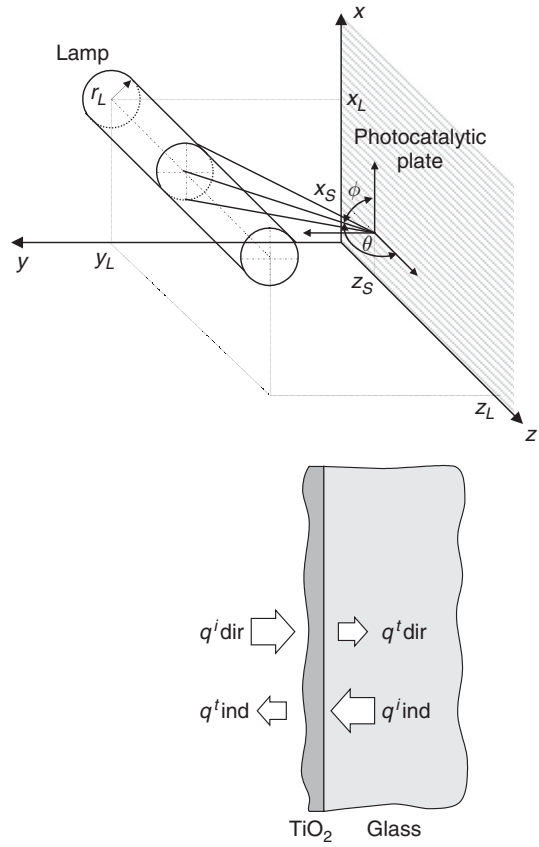

Figure 6 Coordinate system for the radiation model of the laboratory photoreactor.

The limiting values for θ and ϕ can be calculated from geometrical considerations of the lamps and reactor dimensions and their relative positions. The final result is

$$
\begin{aligned}
e^{a,s}(x,z) = {} & \frac{P_{\lambda,L}}{2\pi^2 R_L Z_L} \sum_{\lambda} \sum_{\ell=1}^{7} \int_{\theta} \int_{\phi} \exp\left(-\frac{\kappa_{\lambda,a} e_a}{\cos\theta_n}\right) \left[1 - \exp\left(-\frac{\kappa_{\lambda,f} e_f}{\cos\theta_n}\right)\right] \\
& \times \sin^2\phi \sin\theta \, \mathrm{d}\phi \, \mathrm{d}\theta \\
& + \frac{P_{\lambda,L}}{2\pi^2 R_L Z_L} \sum_{\lambda} \sum_{\ell=8}^{14} \int_{\theta} \int_{\phi} \exp\left(-\frac{\kappa_{\lambda,a} e_a}{\cos\theta_n} - \frac{\kappa_{\lambda,g} e_g}{\cos\theta_n} - \frac{\kappa_{\lambda,f} e_f}{\cos\theta_n}\right) \\
& \times \left[1 - \exp\left(-\frac{\kappa_{\lambda,f} \, e_f}{\cos\theta_n}\right)\right] \sin^2\phi \sin\theta \, \mathrm{d}\phi \, \mathrm{d}\theta
\end{aligned}
\tag{14}
$$

2.3. Kinetics results

The photocatalytic degradation of PCE was studied in the laboratory photoreactor depicted in Figure 5, for different values of PCE inlet concentrations, relative humidities, and irradiation levels (Imoberdorf et al., 2005). It was experimentally found that the PCE reaction rate shows (i) first-order kinetics with respect to the PCE concentration in the gas phase, (ii) linear dependence with respect to the irradiation level, and (iii) site-competitive kinetics for the dependence with the relative humidity. Thus, Equation (7) is reduced to a rather simple analytic expression:

$$\mathsf{R}_{\mathrm{PCE}}(\underline{\mathrm{x}},t) = -\alpha \frac{[\mathrm{PCE}(x,t)]_{\mathrm{gas}}}{1+K_W[\mathrm{H_2O}(x,t)]_{\mathrm{gas}}}\, e^{a,s}(\underline{\mathrm{x}},t) \tag{15}$$

with

$$\alpha = \frac{\alpha_1\alpha_2\bar{\Phi}}{2} = \frac{k_7 K_{\mathrm{PCE}}[\mathrm{Sites}]\bar{\Phi}}{k_{16}[\mathrm{M}]} \tag{16}$$

Comparing the experimental data with the kinetic model (reaction scheme, mass balance, and radiation model) and resorting to a nonlinear regression procedure, the kinetic parameters can be obtained. The results are given in Table 3. Figure 7 shows the quality of the results.

2.4. Pilot scale reactor

The reactor is sketched in Figure 8 where three concentric annular spaces with the six catalytic walls are shown. The reactor is fed through the outer annular space (maximum PCE concentration) where the radiation field has its minimum value. Exit of reactants and products occurs from the inner annular space. All details of the reactor assembly and operating conditions are described in Table 2. For more details the reader can resort to references (Imoberdorf et al., 2006, 2007).

2.5. Reactor model

In this case the reactor is very different and it operates in a continuous fashion. Under the employed experimental conditions the maximum

Table 3 Reaction kinetic parameters for PCE decomposition

Parameter	Value	95% Confidence interval	Units
α	1.54×10^8	0.19×10^8	$\mathrm{cm^3\ Einstein^{-1}}$
K_w	3.21×10^{-4}	0.48×10^{-4}	$\mathrm{m^3\ mg^{-1}}$

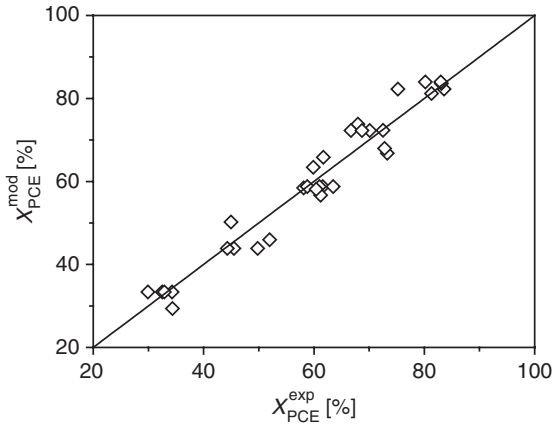

Figure 7 Experimental and predicted outlet conversions for the laboratory photoreactor.

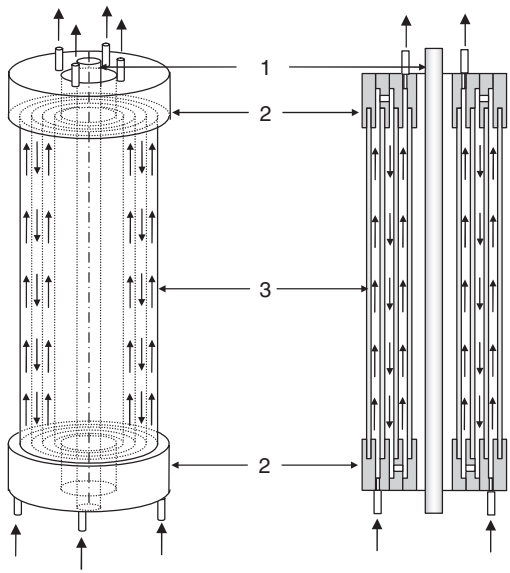

Figure 8 Schematic representation of the pilot scale photocatalytic reactor. Keys: (1) UV lamp, (2) distribution heads, (3) borosilicate glass tubes.

Reynolds number was 25. Therefore, the reactor is operating under well-defined laminar flow conditions. It is also clear that diffusive fluxes of PCE (the only species that experiments significant changes in concentration) can

not affect the velocity profile because of the very low contaminant concentrations. The velocity profile for the j annular space results

$$v_{z,j}(r) = (-1)^{j+1}\frac{2Q}{\pi R_j^2}\frac{\ln \chi_j}{\left[\left(1-\chi_j^4\right)\ln \chi_j + \left(1-\chi_j^2\right)^2\right]} \times \left[1-\left(\frac{r}{R_j}\right)^2 - \frac{\left(1-\chi_j^2\right)}{\ln \chi_j}\ln\left(\frac{r}{R_j}\right)\right] \quad j=1,\ 2,\ 3 \tag{17}$$

It can be noticed that the momentum balance was not required in the laboratory reactor due to its particular operating conditions.

The mass transfer equation is written in terms of the usual assumptions. However, it must be considered that because the concentration of the more abundant species in the flowing gas mixture (air), as well as its temperature, are constant, all the physical properties may be considered constant. The only species that changes its concentration along the reactor in measurable values is PCE. Therefore, the radial diffusion can be calculated as that of PCE in a more concentrated component, the air. This will be the governing mass transfer mechanism of PCE from the bulk of the gas stream to the catalytic boundaries and of the reaction products in the opposite direction. Since the concentrations of nitrogen and oxygen are in large excess they will not be subjected to mass transfer limitations. The reaction is assumed to occur at the catalytic wall with no contributions from the bulk of the system. Then the mass balance at any point of the reactor is

$$\frac{\partial C_{\mathrm{PCE}}(r,z)}{\partial z}v_{z,j}(r) = \frac{D^0_{\mathrm{PCE-Air}}}{r}\frac{\partial}{\partial r}\left(r\frac{\partial C_{\mathrm{PCE}}(r,z)}{\partial r}\right) \quad (0<z<Z_R;\quad \chi_j R_j < r < R_j;\quad j=1,2,3) \tag{18}$$

with the boundary conditions:

$$D^0_{\mathrm{PCE-Air}}\left.\frac{\partial C_{\mathrm{PCE}}(r,z)}{\partial r}\right|_{r=R_j} = \mathsf{R}_{\mathrm{PCE}}[C_{\mathrm{PCE}}(R_j,z), C_{\mathrm{H_2O}}, e^{a,s}(R_j,z)] \quad (0<z<Z_R;\quad j=1,2,3)$$

$$D^0_{\mathrm{PCE-Air}}\left.\frac{\partial C_{\mathrm{PCE}}(r,z)}{\partial r}\right|_{r=\chi_j R_j} = -\mathsf{R}_{\mathrm{PCE}}[C_{\mathrm{PCE}}(\chi_j R_j,z), C_{\mathrm{H_2O}}, e^{a,s}(\chi_j R_j,z)] \quad (0<z<Z_R;\quad j=1,2,3) \tag{19}$$

$$
\begin{aligned}
C_{\mathrm{PCE}}(r,z)\big|_{z=0} &= C^0_{\mathrm{PCE}}; && (\chi_3 R_3 < r < R_3)\\
C_{\mathrm{PCE}}(r,z)\big|_{z=Z_R} &= \frac{\displaystyle\int_{\chi_3 R_3}^{R_3} C_{\mathrm{PCE}}(r,Z_R)\,v_{z,3}(r)\,r\mathrm{d}r}{\displaystyle\int_{\chi_3 R_3}^{R_3} v_{z,3}(r)\,r\mathrm{d}r}; && (\chi_2 R_2 < r < R_2)\\
C_{\mathrm{PCE}}(r,z)\big|_{z=0} &= \frac{\displaystyle\int_{\chi_2 R_2}^{R_2} C_{\mathrm{PCE}}(r,0)\,v_{z,2}(r)\,r\mathrm{d}r}{\displaystyle\int_{\chi_2 R_2}^{R_2} v_{z,2}(r)\,r\mathrm{d}r}; && (\chi_1 R_1 < r < R_1)
\end{aligned}
\tag{20}
$$

It can be observed that the differences between the set of Equations (18)–(20) with respect to Equation (8) are evident. It is also important to recognize that in this mathematical modeling it can be observed the correct formulation of the nature of the catalytic wall reaction and its spatial dependence with respect to the position variables.

The PCE conversion at the reactor outlet is calculated with the mixing cup average concept:

$$
X_{\mathrm{PCE}}[\%] = \left(1 - \frac{\displaystyle\int_{\chi_1 R_1}^{R_1} C_{\mathrm{PCE}}(r,Z_R)\,v_{z,1}(r)\,r\mathrm{d}r}{C^0_{\mathrm{PCE}}\displaystyle\int_{\chi_1 R_1}^{R_1} v_{z,1}(r)\,r\mathrm{d}r}\right)\times 100 \tag{21}
$$

At this point a third important difference must be noticed. The value of $\mathsf{R}_{\mathrm{PCE}}$ in Equation (19) is not exactly equal to Equation (15) because the value of $e^{a,s}$ will be utterly different from one reactor and the other. This aspect will be considered in the next section.

2.6. The radiation field

The concepts employed in developing Equations (11)–(14) can be described in a simpler way here, because this reactor has a single lamp (Figure 9). The calculus of the LSRPA is made as follows:

$$
e^{a,s}_{\lambda}(r,z) = q^{i}_{\lambda}(r,z) - q^{t}_{\lambda}(r,z) \tag{22}
$$

with

$$
q_{\lambda}(r,z) = \int_{\phi_{\min}(r)}^{\phi_{\max}(r)} \int_{\theta_{\min}(r,z,\phi)}^{\theta_{\max}(r,z,\phi)} I_{\lambda,L}\,\cos\phi\,\sin^2\theta\,\mathrm{d}\theta\mathrm{d}\phi \tag{23}
$$

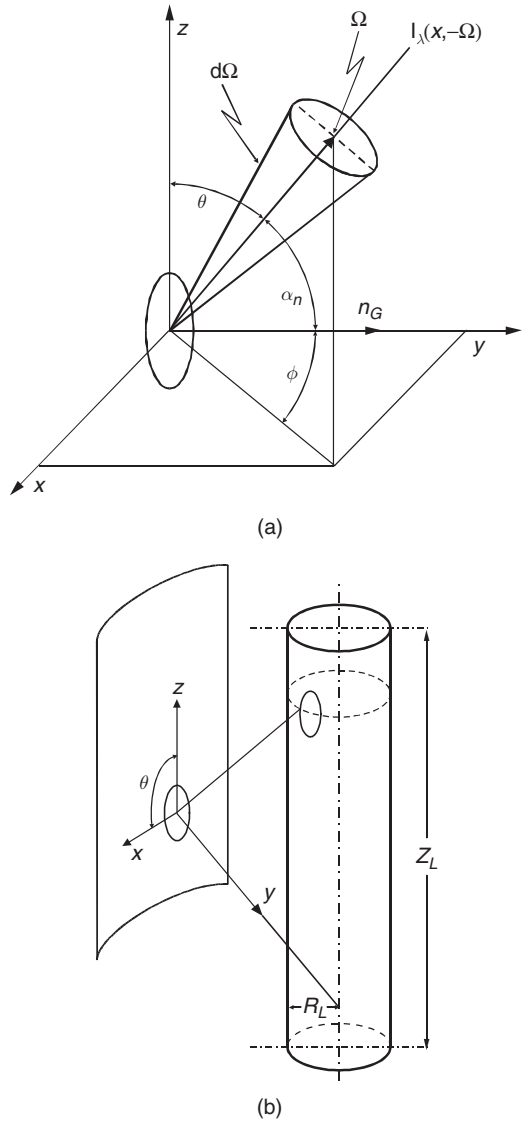

Figure 9 Coordinate system for the radiation model of the pilot scale photoreactor. Adapted from Imoberdorf et al. (2006).

where the limits are defined by the dimensions of the lamp contour as seen from the point of incidence according to the relative distances between the lamp and the reactor (Figure 9):

$$\theta_{\min}(r,z,\phi) = \tan^{-1}\left\{\frac{r\cos\phi - [R_L^2 - r^2\sin^2\phi]^{1/2}}{(Z_L - z)}\right\} \tag{24}$$

$$\theta_{\max}(r,z,\phi) = \tan^{-1}\left\{\frac{r\cos\phi - [R_L^2 - r^2\sin^2\phi]^{1/2}}{z}\right\} \tag{25}$$

$$\phi_{\min} = -\cos^{-1}\left[\frac{(r^2 - R_L^2)^{1/2}}{r}\right] \qquad \phi_{\max} = \cos^{-1}\left[\frac{(r^2 - R_L^2)^{1/2}}{r}\right] \tag{26}$$

And the boundary conditions result

$$I_\lambda(r,z,\phi,\theta) = \begin{cases} 0 & (\phi,\theta) < (\phi_{\min}) \\ I_{\lambda,L} & = \dfrac{P_{\lambda,L}}{2\pi^2 R_L Z_L} \quad (\phi_{\min}) < (\phi,\theta) < (\phi_{\max}) \\ 0 & (\phi_{\max}) < (\phi,\theta) \end{cases} \tag{27}$$

The value of the LSRPA in the thin catalytic film is finally obtained as follows (Table 4):

$$\begin{aligned} e^{a,s}(r,z) = \frac{P_{\lambda,L}}{2\pi^2 R_L Z_L} & \sum_{\lambda=300\text{ nm}}^{420\text{ nm}} \int_{\phi_{\min}(r)}^{\phi_{\max}(r)} \int_{\theta_{\min}(r,z,\phi)}^{\theta_{\max}(r,z,\phi)} \\ & \times \exp\left(-n_g(r)\frac{\kappa_{\lambda,g}e_g}{\cos\alpha_n} - n_f(r)\frac{\kappa_{\lambda,f}e_f}{\cos\alpha_n}\right) \\ & \times \left[1 - \exp\left(-\frac{\kappa_{\lambda,f}e_f}{\cos\alpha_n}\right)\right]\cos\phi\,\sin^2\theta\,\mathrm{d}\theta\mathrm{d}\phi \end{aligned} \tag{28}$$

Variables are defined in the nomenclature section. Differing from the case of the flat plate reactor where the radiation field in the employed part of the surface was almost uniform (differences were never larger than 9%), in this reactor the whole system exhibit only azimuthal symmetry and significant differences were observed in both directions (r, z). However, even more

Table 4 Keys to interpret the values of the parameters employed in Equation (28)

Geometry of the multiannular reactor	Space #	n_g (r)	n_f (r)
First annular space. Inner radius	1	1	0
First annular space. Outer radius	1	1	1
Second annular space. Inner radius	2	2	2
Second annular space. Outer radius	2	2	3
Third annular space. Inner radius	3	3	4
Third annular space. Outer radius	3	3	5

important is the contrast of the LSRPA between the value in the inner annulus and the outer one. This result must be used in Equation (19).

2.7. Validation

The experimental conversion is calculated according to

$$X_{PCE}\% = \frac{C_{PCE}^{in} - C_{PCE}^{out}}{C_{PCE}^{in}} \times 100 \tag{29}$$

Experimental values obtained in this way must be compared with those calculated according to Equation (21). Predicted versus experimental values are compared in Figure 10. The root mean square error (RMSE) is less than 5.6%. It should be noted that no adjustable parameters have been employed and the method can be used for any reactor size without limitations.

As mentioned in Imoberdorf et al. (2007) it is very difficult that a practical application will use annular spaces thicker than the ones employed in this reactor without producing mass transfer limitations. Similar effects should be expected if lamps of larger output power were employed. It is also apparent that no additional annular spaces are needed because almost no UV radiation is transmitted by the outer reactor tube. The only variables that are available to the design engineers are (i) the reactor length Z_R, (ii) the flow rate, taken into account by v_z, and (iii) larger lamps (defined by $P_{\lambda,L}$, R_L, and Z_L). All these variables are included in the design equations previously presented in Sections 2.5 and 2.6 of this work.

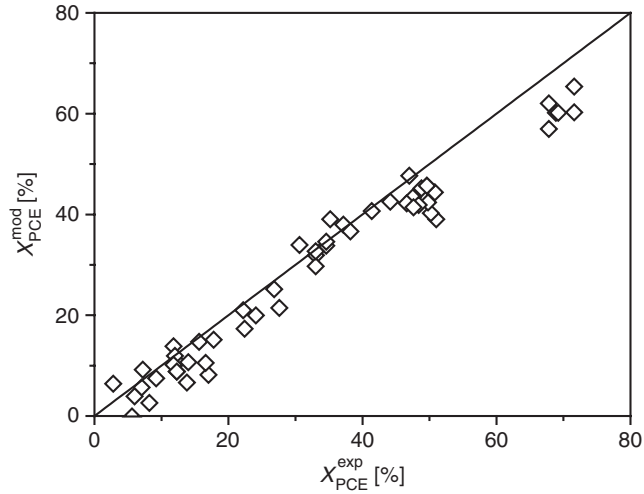

Figure 10 Experimental and predicted outlet conversions for the pilot scale photoreactor.

3. SCALING-UP OF A HOMOGENEOUS PHOTOCHEMICAL REACTOR WITH RADIATION ABSORPTION

This case will be illustrated with a rather simple reaction in liquid phase: the decomposition of low concentrations of formic acid in aqueous solutions employing hydrogen peroxide and UVC radiation (253.7 nm). Formic acid is a byproduct of the degradation of many organic compounds (Labas et al., 2002).

3.1. Reaction scheme and kinetic model

The same considerations made before are valid for this case and it is very important to have an available validated reaction mechanism. It can be obtained from three main sources (Blelski et al., 1985; Buxton et al., 1988; Stefan and Bolton, 1998) and it is shown in Table 5. With the available information about the constant k_2, k_3, k_5, k_6, and k_7, it could be possible to solve a system of four differential equations and extract from the experimental data, the missing constants ϕ and k_4 (that in real terms is $k_4^\star/C_{O_2}$). This method would provide good information about the kinetic constants, but it is not the best result for studying temperature effects if the same information is not available for the pre-exponential factors and the activation energies. Then, it is better to look for an analytical expression even if it is necessary to make some approximations. This is particularly true in this case, where the direct application of the micro steady-state approximation (MSSA) is more difficult due to the existence of a recombination step that includes the two free radicals formed in the reaction. From the available information, it is possible to know that to calculate the pseudo-steady-state

Table 5 Proposed kinetic scheme for formic acid mineralization

Activation	
$H_2O_2 + h\nu \rightarrow 2OH\bullet$	ϕ
Main reaction	
$H_2O_2 + OH\bullet \rightarrow HO_2\bullet + H_2O$	k_2
$HO_2\bullet + H_2O_2 \rightarrow H_2O + O_2 + OH\bullet$	k_3
$OH\bullet + HCOOH \xrightarrow{C_{O_2}} CO_2 + H_2O + HO_2\bullet$	k_4
Termination steps	
$HO_2\bullet + OH\bullet \rightarrow H_2O + O_2$	k_5
$HO_2\bullet + HO_2\bullet \rightarrow H_2O_2 + O_2$	k_6
$OH\bullet + OH\bullet \rightarrow H_2O_2$	k_7

$k_4 = k_4^\star/C_{O_2}$; C_{O_2} = constant $\cong$ 7.5–8.0 ppm.
Adapted from Labas et al. (2002).

concentration of the OH· radicals, a good presumption is to consider that step 5 can be neglected (because k_5 and HO_2· are relatively small), but the same cannot be done to calculate the concentration of HO_2·. Also, it is widely recognized (Buxon et al., 1988; Stefan and Bolton, 1998) that the main attack to formic acid is produced by the OH· radical as compared with the one produced by the HO_2· radical. Applying the MSSA the following equations are obtained:

$$\mathsf{R}_F = -\frac{\phi e^a_\lambda}{1/2 + r(\alpha_1)} \tag{30}$$

$$\mathsf{R}_P = -\phi e^a_\lambda - \frac{\phi e^a_\lambda}{1 + (1/\alpha_1)^{\frac{1}{r}}} \tag{31}$$

where $r = C_P/C_F$ and $\alpha_1 = k_4/k_2$. Here $e^a_\lambda(\underline{x}, t)$ is the LVRPA a function of position and time because (i) the radiation field is intrinsically not uniform and the radiation absorbing species concentration changes with time. In this case, since there is no direct photolysis of formic acid (negligible radiation absorption at 253.7 nm) the chemical species that is responsible for the initiation reaction is hydrogen peroxide (see Table 5).

3.2. Laboratory reactor: description and modeling

It is always important to design a laboratory reactor that has the simplest mathematical representation for both the mass and the radiation balance. In this case the work was carried out in a flat plate reactor with circular windows made of quartz. A removable shutter permits to obtain steady-state operation of the whole system (including lamps) before the run commences. The start of the reaction ($t = 0$) occurs when it is taken off. Other features are described in Figures 11 and 12 and Table 6. Details on all the experimental procedure can be found in Labas et al. (2002).

A simple mass balance can be obtained for the recycling system when the following conditions are fulfilled: (i) the whole system operates under well-stirred conditions, (ii) the ratio V_R/V_T is $<< 1$, and (iii) the recirculating flow rate is high such as to have differential conversion per pass in the photoreactor and, at the same time, improve mixing. Then, it can be shown (Cassano and Alfano, 2000) that the changes in concentration in the tank are related to the reaction rates according to Equations (30) and (31)

$$\left.\frac{dC_j(t)}{dt}\right|_{\text{Tank}} = \frac{V_R}{V_T}\langle \mathsf{R}_{\text{Hom.},j,\lambda}\ (\underline{x}, t)\rangle_{V_R} \tag{32}$$

With the initial condition that $C_j(t = 0) = C_j^0$

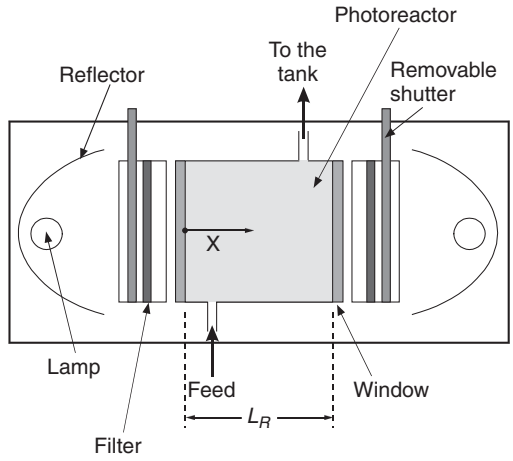

Figure 11 Laboratory reactor.

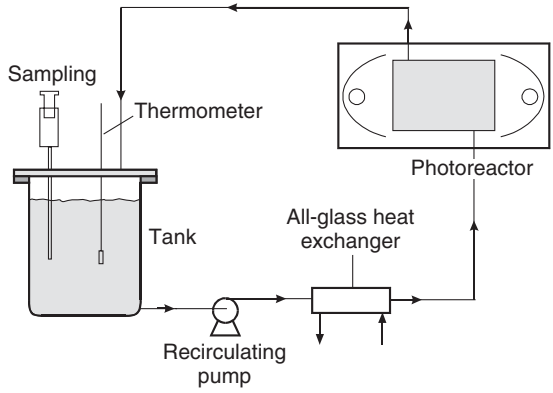

Figure 12 Schematic representation of laboratory reactor set-up.

In spite of the prevailing well-stirred conditions, since the radiation field is not uniform, the volume average of the homogeneous rate must be calculated. It will be seen in what follows, that the significant variable is x and the averaging integral is

$$\langle \mathsf{R}_{\mathrm{Hom.},j,\lambda}\ (\underline{\mathrm{x}},t)\rangle_{V_R} = \langle \mathsf{R}_{\mathrm{Hom.},j,\lambda}(x,t)\rangle_{L_R} = \frac{1}{L_R}\int_{L_R} \mathsf{R}_{\mathrm{Hom.},j,\lambda}(x,t)\mathrm{d}x \qquad (33)$$

The reaction rate requires the evaluation of the LVRPA. In the absence of emission and scattering, the transport of photons in the

Table 6 Laboratory and pilot scale reactor description and operating conditions

Item	Specification/Dimensions	
	Laboratory reactor	Pilot scale reactor
Type	Flat plate. Batch, with a recycle. Two circular windows made of quartz, Suprasil quality	Annular shape. Continuous flow, tubular reactor in two sections of one meter each
Total reactor volume	69.9 cm^3	13,000 cm^3
Dimensions	Two sides. Each: $D = 4.26$ cm	$Z_R = 200$ cm, $R_{int} = 2.4$ cm, $R_{ext} = 5.35$ cm
	$L_R = 4.9$ cm	$R_{R,int} = 2.5$ cm, quartz $R_{R,ent} = 5.2$ cm
Lamps	One in each side	Two. One in each reactor section Philips TUV 40 W each.
Germicidal	Philips TUV 15 W Heraeus UV-C 40 W	Output power: 0.105 W cm^{-1} Total output power: 25.2 W
Almost monochromatic	Philips TUV 15 W with filter	Used output power: 21 W $Z_{L,tot} = 2 \times 120$ cm, $Z_{L,used:}$ 2×100 cm $R_L = 1.3$ cm
Wavelength	(90%) $\lambda = 253.7$ nm	(90%) $\lambda = 253.7$ nm
Reflectors	Parabolic cylinder. Made of Aluminum, specularly finished	None
Incident radiation at the wall	Measured by actinometry (potassium ferrioxalate) $(13.9–5.45–2.33) \times 10^{-9}$ Einstein cm^{-2} s^{-1}	Calculated with a volumetric emission model

Table 6 (*Continued*)

Item	Specification/Dimensions	
	Laboratory reactor	Pilot scale reactor
Operation		
Flow rate	Batch, with recirculation: 2,000 cm^3 min^{-1}	Continuous: 1,500–5,000 cm^3 min^{-1}
Temperature	20°C	20°C
Pressure	1 atm	1 atm
Inlet COOH concentration	40–140 ppm	46–110 ppm
Inlet H_2O_2 concentration	Molar ratio: 1–32	Molar ratio: 2–7.5

reaction space is given by Equation (34) and the appropriate boundary conditions.

$$\underbrace{\frac{dI_{\lambda,\underline{\Omega}}(\underline{x},t)}{ds}}_{\substack{\textit{Changes}\ \text{in}\ I_{\lambda,\underline{\Omega}}\ \text{along}\\ \text{the distance ds in a}\\ \textit{three}\text{-dimensional space}}} + \underbrace{\kappa_\lambda(\underline{x},t)I_{\lambda,\underline{\Omega}}(x,t)=0}_{\substack{\textit{Radiation}\ \text{absorption}\\ \text{along ds}}} \tag{34}$$

with the boundary condition that at $s = 0 \rightarrow I_{\lambda,\underline{\Omega}}(\underline{x},t) = I^0_{\lambda,\underline{\Omega}}(\underline{x},t)$.

It has been shown that under some geometric restrictions that involve conditions in distances and dimensions of the complete experimental device; that is, lamps, reflectors, and reactors, the radiation field produced by the tubular lamp, and the parabolic reflector can be modeled by a one-dimensional representation (Alfano et al., 1986). These limitations were imposed on the equipment design of this work. Since κ_λ is a function of the radiation-absorption species concentration, in this case, Equation (34) is coupled with Equation (32).

When Equation (34) is solved, monochromatic specific intensities are obtained. From these values, the monochromatic incident radiation G_λ (photons of a given energy per unit normal area of incidence, unit time, and unit wavelength interval) and the monochromatic LVRPA $e^a_{j,\lambda}$ (absorbed photons of a given energy by the intervening radiation absorption species, per unit reaction volume, unit time and unit wavelength interval) can be readily calculated according to Equations (35) and (36), respectively. No direct photolysis of formic acid (F) was observed; then, in this case, j is just H_2O_2 (P).

$$G_\lambda(x,t) = \int_\Omega I_{\lambda,\underline{\Omega}}(x,t)d\Omega \tag{35}$$

Note that in calculating G_λ all possible radiation absorbing species must be counted; for example, if inner filtering effects are present they must be included.

$$e^a_\lambda(x,t) = \kappa_{\lambda,P}(x,t)\ G_\lambda(x,t) \tag{36}$$

In Equation (36) the subscript P was included to indicate that in calculating the LVRPA from the value of $G(x, t)$ only the absorption coefficient of the reactant radiation absorbing species must be included. When Equation (36) is averaged over the reactor volume, it renders the required expression for Equation (32). This direct substitution is possible only because the reactor is assumed to be well mixed and concentrations are uniform, taking on a

single spatial value (resulting from a hydrodynamic average). Since monochromatic radiation is used, no integration over wavelengths is necessary.

The final local result for $e^a_\lambda(x,t)$ is

$$e^a_\lambda(x,t) = \kappa_{\lambda,P} G_{w,\lambda} \left\{ \exp\left[-\left(\sum_j \kappa_{\lambda,j}(t) \right) x \right] + \exp\left[-\left(\sum_j \kappa_{\lambda,j}(t) \right) (L_R - x) \right] \right\} \tag{37}$$

In this particular case, j is also equal to P. As indicated in Equation (34), the solution of the problem requires the evaluation of the boundary condition. In the one-dimensional model, this requisite is translated into the evaluation of $G_{w,\lambda}(x,\ t)$ as shown in Equation (37). Thus G_w at $x = 0$ and $x = L_R$ must be known.

For a laboratory reactor like the one used in this work, these values can be obtained resorting to conventional actinometry employing the well-known potassium ferrioxalate reaction. The details of the method can be found in Zalazar et al. (2005). The obtained results for the boundary conditions are indicated in Table 6.

3.3. Kinetic results

The experimental data were used to extract from the modeling Equations (30) and (31) the values of the parameters. For this purpose, a multiparameter, nonlinear estimator was used. It turns out that resulting from these estimations, the equations can be further simplified for $r < 50$ (a conservative assumption), rendering:

$$\mathsf{R}_F(x,t) = -2\,\phi\, e^a_\lambda(x,t) \tag{38}$$

$$\mathsf{R}_P(x,t) = -\alpha_1\,\phi\, e^a_\lambda(x,t) r(t) \tag{39}$$

The final estimation gives the following results with a 95% confidence interval:

$\phi = 0.372 \pm 0.0114$ Einstein mol^{-1}
$\alpha_1 = 6.67 \times 10^{-3} \pm 1.86 \times 10^{-3}$(dimensionless).

Figure 13a, b shows two typical outcomes where the solid lines are the theoretical simulations from the simplified model. These parameters can be now applied to the large-scale reactor and, as before, a new value of the LVRPA will be necessary according to its particular configuration.

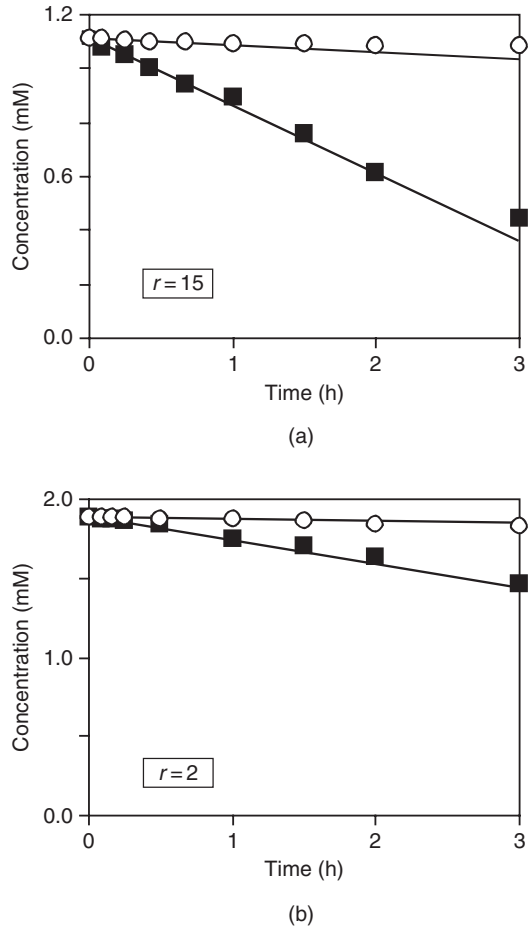

Figure 13 Typical results of laboratory experiments and results from the model (solid lines). (a) $r = 25$, (b) $r = 2$. (○) Hydrogen peroxide, (■) formic acid.

3.4. Pilot scale reactor

The larger reactor operates under a steady state, continuous flow conditions and was made of two 1 m cylindrical reactors of annular shape in order to use conventional Germicidal lamps (Figure 14). The system of tanks shown in the flow sheet was used to (i) feed the reactor with a constant flow rate and (ii) wash the system after each experimental run. The actual operating length (Z_L) of each lamp (1.2 m long) was 1 m. Operation could be made with just one reactor or the two in series.

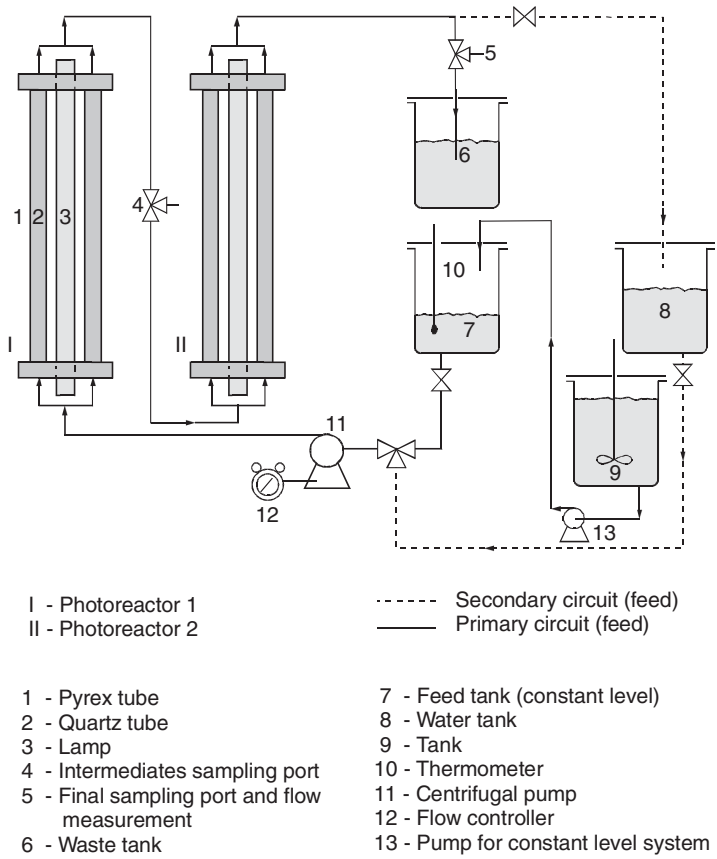

Figure 14 Schematic representation of pilot size setup for a continuous flow reactor.

3.5. Reactor model

The momentum balance is similar to the one used in Section 2.5 but for a single annular space:

$$v_z(r) = \frac{\Delta P R_{R,\text{ext}}^2}{4\mu Z_R}\left[1 - \left(\frac{r}{R_{R,\text{ext}}}\right)^2 + \left(\frac{1-\chi^2}{\ln(1/\chi)}\right)\ln\left(\frac{r}{R_{R,\text{ext}}}\right)\right] \tag{40}$$

In this equation $\chi = R_{R,\text{int}}/R_{R,\text{ext}}$.

For the mass balance, the following assumptions and operating conditions are considered: (i) steady state, (ii) unidirectional, incompressible, continuous flow of a Newtonian fluid under laminar flow regime, (iii) only ordinary diffusion is significant for a mixture where the main component is water, (iv) azimuthal symmetry, (v) axial diffusion neglected as

compared to the convective flow, and (vi) constant physical and transport properties. The following model equation in cylindrical coordinates (r, z) holds:

$$v_z(r)\frac{\partial C_i(z,r)}{\partial z} - D_{i,\text{water}}\left[\frac{1}{r}\frac{\partial}{\partial r}\left(r\frac{\partial C_i(z,r)}{\partial r}\right)\right] = \mathsf{R}_{\text{Hom},i}\ (z,r), \quad i = P,F \tag{41}$$

Note the difference between this equation and Equation (18). In this case, the homogeneous reaction is a part of the differential equation. Equation (41) must be integrated with the following initial and boundary conditions:

$$z = 0 \quad R_{R,\text{int}} \le r \le R_{R,\text{ext}} \quad C_i = C_{i,0} \tag{42}$$

$$r = R_{R,\text{int}} \quad 0 \le z \le Z_R \quad \frac{\partial C_i}{\partial r} = 0 \tag{43}$$

$$r = R_{R,\text{ext}} \quad 0 \le z \le Z_R \quad \frac{\partial C_i}{\partial r} = 0 \tag{44}$$

In the right-hand side of Equation (41), we must insert the results of the kinetic model, that is, Equations (38) and (39) with the kinetic parameters obtained in the laboratory reactor. The solution of the partial differential equation provides formic acid and hydrogen peroxide exit concentrations as a function of the radial position.

3.6. Radiation model

As in Section 2.6, in order to use Equations (38) and (39) in Equation (41) a model for the photon distribution in the annular space is needed. In this case, no actinometric methods can be applied because, in the general case, the reactor cannot be built before the design is completed; that is, there is no equipment to make the measurements and, consequently, no experimental data concerning the incoming radiation are available. Thus, an emission model must be used. It can be obtained with the three-dimensional source with volumetric emission model, the TDSVE Model and the ray tracing technique (Cassano et al., 1995; Irazoqui et al., 1976; Siegel and Howell, 2002). It is necessary to know the optical characteristics of the reactor wall, the optical characteristics of the reaction space and the geometrical dimensions of the lamp–reactor system.

The emission model is based on the following assumptions: (1) the lamp has an extension given by its used length (Z_L) and its radius (R_L); in this extension, emitters are uniformly distributed. (2) Each elementary volume of the lamp is an emitter. The specific intensity associated with each bundle of radiation coming from each emitter, at each wavelength, is spherical,

isotropic, and proportional to its extension. (3) Each elementary differential volume of the lamp is transparent to the energy emerging by each emitter located in its surroundings. (4) The lamp is a perfect cylinder whose boundaries are mathematical surfaces without thickness. (5) In this case, end effects in the lamp electrodes are avoided; that is, the used length is shorter that the lamp length. (6) A spherical coordinate system located at each point of radiation reception (I_n)inside the reactor can characterize the arriving specific intensity. It is necessary to know the distance from such point to the centerline of the lamp and two pairs of angular coordinates $[(\theta_{\max}, \theta_{\min}); \quad (\phi_{\max}, \phi_{\min})]$ that define the extension of the useful volume of the lamp. (7) The radiant power of the lamp (P, in units of Einstein s^{-1}) can be calculated knowing the dimensions of the lamp and the isotropic characteristics of its emission.

Figure 15a shows the emission along the direction (θ,ϕ) produced by a small volume element of the lamp with volumetric emission that reaches the reactor at $s = s_R$. Looking at Figure 15a, Equation (34) can be integrated along this given direction of propagation (defined by the θ and ϕ coordinates) from $s = s_R$ (at an arbitrary point on the surface of radiation entrance to the reactor) to a point of incidence I_n inside the reactor

$$I_\lambda\,(\underline{x},\ \theta,\ \phi, t)\ =\ I^0_\lambda\,(\theta,\ \phi, t)\ \exp\left[-\int_{\bar{s}=s_R(\underline{x}_0,\theta,\phi)}^{\bar{s}=s_I(\underline{x},\theta,\phi)} \kappa_{\lambda,p}(\bar{s}, t)\mathrm{d}\bar{s}\right] \tag{45}$$

where $I^0_\lambda\,(\theta, \phi, t) = I_\lambda\,(s_R, \underline{\Omega}, t)$ is the boundary condition for I_λ at the point of entrance and for an arbitrary direction $\underline{\Omega}$. This boundary condition is provided by the lamp emission model. For steady irradiation and the listed assumptions, the result is

$$I^0_\lambda(\theta, \phi) = \frac{P_{\lambda,L}}{4\pi^2 R_L^2 Z_L}\frac{(R_L^2 - r^2\ \sin^2\phi)^{1/2}}{\sin\theta} Y_{\lambda,R}(\theta, \phi) \tag{46}$$

In Equation (46)$Y_{\lambda,R}$ is a compounded transmission coefficient of the reactor wall (considering absorption and reflections). The value of $P_{\lambda,L}$ was verified with radiometer measurements. Equations (45) and (46) give the radiation contribution of an arbitrary direction (θ,ϕ) to the point $I_n(\underline{x}, \theta, \phi)$ inside the reactor. The next step is to integrate all possible directions of irradiation from the lamp volume of emission to the point I_n (Figure 15b).

According to Cassano et al. (1995), knowing the value of the specific intensity at each point, the value of the Incident Radiation $\left[G_\lambda(\underline{x}) = \int_\Omega I_\lambda(\underline{x}, \underline{\Omega})\mathrm{d}\Omega\right]$ at a point $\underline{x}$ inside the reactor, is obtained by integration over the solid angle of incidence ($\mathrm{d}\Omega = \sin\theta \mathrm{d}\theta\mathrm{d}\phi$). The limits

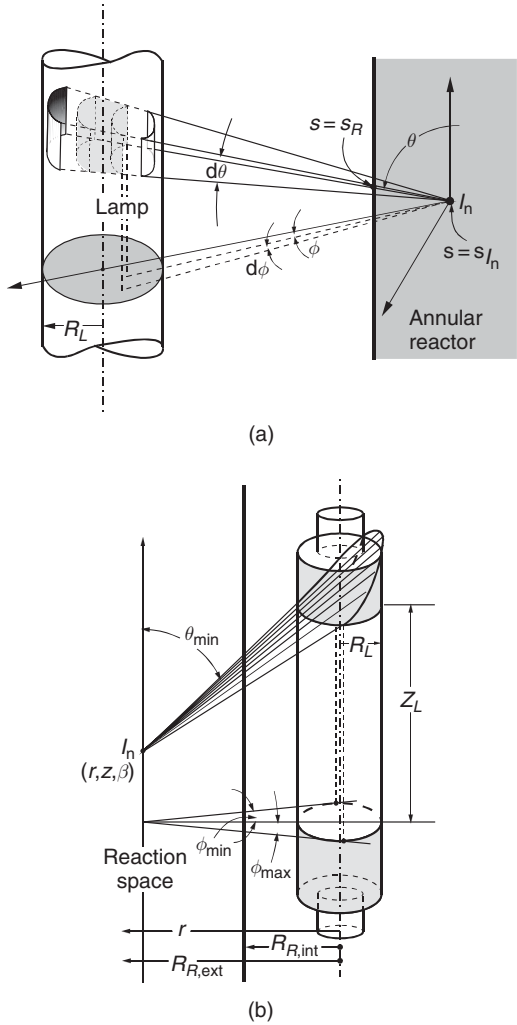

Figure 15 (a) Emission model for the volumetric lamp. (b) Limits of integration for the lamp contour.

for the integration are obtained from the lamp model, according to the dimensions of the radiation source, defined by the spherical coordinates $[(\theta_{\max}, \theta_{\min}); \quad (\phi_{\max}, \phi_{\min})]$:

$$G_\lambda(\underline{x}, t) = \int_{\phi_{\min}}^{\phi_{\max}} \mathrm{d}\phi \int_{\theta_{\min}(\phi)}^{\theta_{\max}(\phi)} \mathrm{d}\,\theta \sin\theta\, I^0_{\lambda,\underline{\Omega}}\,(\theta, \phi, t) \exp\left[- \int_{\bar{s}=s_R(\underline{x}_0,\theta,\phi)}^{\bar{s}=s_I(\underline{x},\theta,\phi)} \kappa_\lambda(\bar{s}, t)\mathrm{d}\bar{s} \right] \tag{47}$$

In the double integral θ accounts for the lamp length and ϕ for the lamp diameter. The integration limits are given by Equations (24)–(26).

Finally, at any point inside the annular reaction space, the LVRPA is

$$e^a_\lambda(\underline{x},t) = \kappa_\lambda(\underline{x},t)\int_{\phi_{\min}}^{\phi_{\max}} d\phi \int_{\theta_{\min}(\phi)}^{\theta_{\max}(\phi)} d\theta \sin\theta\, I^0_{\lambda,\underline{\Omega}}(\theta,\phi,t)$$
$$\times \exp\left[-\int_{\bar{s}=s_R(\underline{x}_0,\theta,\phi)}^{\bar{s}=s_I(\underline{x},\theta,\phi)} \kappa_\lambda(\bar{s},t)d\bar{s}\right] \tag{48}$$

Equation (48) has to be inserted into Equations (38) and (39) to provide the reaction rates for Equation (41).

3.7. Validation

In order to compare these results with data from the actual reactor and considering the velocity distribution of the outgoing flow, the bulk or flow-average concentration of the reactor outgoing stream must be calculated:

$$C_{\text{exit},i} = \frac{\int_{R_{R,\text{int}}}^{R_{R,\text{ext}}} v_z(r)C_i\ (r, z = Z_R)r dr}{\int_{R_{R,\text{int}}}^{R_{R,\text{ext}}} v_z(r)r dr} \tag{49}$$

These values must be compared with the experimental measurements. The results are shown in Table 7. There are some differences and two main reasons to explain some of the discrepancies: (i) the fully developed laminar flow assumption of Equation (40) is not fulfilled and (ii) in the connection between both reactor lengths there is some mixing that has not been taken into account by the model. The problems occurring with the velocity field can certainly be solved without difficulties, substituting Equation (40) by a more realistic velocity distribution inside the reaction space resorting to available CFD programs.

Table 7 Scale-up: predictions versus experiments

Run	C_F (ppm)	r	$X_{\text{Pred.}}$	$X_{\text{Exp.}}$	% error
1	46	2	19.0	17	11.8
2	92	2	19.2	23.5	18.3
3	110	7.5	32.7	35	6.6

$X_F = \frac{C_{F,0} - C_{F,\text{exit}}}{C_{F,0}}$.

In this reactor some additional information should be added to the last paragraph of Section 2.7. In this case, (i) longer (up to 220 cm) and better lamps (having a significant output power at lower wavelengths, where radiation absorption by hydrogen peroxide is stronger) can be used and (ii) wider annular spaces can also be adopted because radiation absorption by H_2O_2 is rather weak. All other observations have the same validity.

4. SCALING-UP OF A HETEROGENEOUS PHOTOCATALYTIC REACTOR WITH RADIATION ABSORPTION AND SCATTERING

This case shows the degradation of 4-chlorophenol (4-CP) employing UVA radiation and Aldrich titanium dioxide catalyst ($S_g = 9.6\,cm^2\,g^{-1}$, nominal diameter of the elementary particle: 200 nm) in a slurry reactor at pH 2.5, which was found to provide the most efficient reaction condition (Satuf et al., 2007a, b, 2008).

4.1. Reaction scheme and kinetic model

The reaction scheme is shown in Table 8 and was constructed on the basis of information existing in the literature, mainly in the following contributions: Turchi and Ollis (1990), Terzian et al. (1990), Minero et al. (1992), Mills et al. (1993), Mills and Morris (1993), Theurich et al. (1996), Alfano et al. (1997), Almquist and Biswas (2001), Dijkstra et al. (2002), and Palmisano et al. (2007) among others. The different reaction steps show the typical characteristics of this heterogeneous reaction: (i) UV catalyst activation, (ii) electron–hole recombination, (iii) hole trapping, (iv) electron trapping, (v) hydroxyl radical attack to 4-CP and the main reaction intermediates along two different routes (Figure 16), and (vi) all the involved adsorption steps indicating that 4-CP and the principal byproducts [4-chlorocatechol (4-CC) and hydroquinone (HQ)] absorb in different catalytic sites than oxygen.

The kinetic model is based on the following assumptions: (i) photocatalytic reactions occur among adsorbed species adsorbed on the catalytic surface, (ii) dynamic equilibrium exits between the bulk and the surface concentrations of adsorbed species, (iii) ·OH radical attack is the main route for all degradation reactions of organic compounds, (iv) the MSSA applies for unstable intermediate species, and (v) there are no mass transfer limitations due to the operating mixing conditions. Most of these assumptions were first proposed and discussed by Turchi and Ollis (1990) for the photocatalytic degradation of several organic water pollutants in TiO_2 slurries and then applied by Cabrera et al. (1997) and Brandi et al. (2002) to obtain a kinetic model of the photocatalytic decomposition of trichloroethylene in aqueous suspensions.

Table 8 Reaction mechanism

Activation	$TiO_2 + h\nu \rightarrow TiO_2 + e^- + h^+$	R_g
Recombination	$e^- + h^+ \rightarrow$ heat	k_2
Electron trapping	$e^- + O_{2,ads} \rightarrow \bullet O_2^-$	k_3
Hole trapping	$h^+ + H_2O_{ads} \rightarrow \bullet OH + H^+$	k_4
	$h^+ + OH^-{}_{ads} \rightarrow \bullet OH$	
Hydroxyl attack	$4\text{-}CP_{ads} + \bullet OH \rightarrow 4\text{-}CC$	k_5
	$4\text{-}CP_{ads} + \bullet OH \rightarrow HQ$	k_6
	$4\text{-}CC_{ads} + \bullet OH \rightarrow X_i$	k_7
	$HQ_{ads} + \bullet OH \rightarrow X_j$	k_8
	$Y_{In,ads} + \bullet OH \rightarrow Y_m$	k''_{In}
Adsorption	$site_{O_2} + O_2 \leftrightarrow O_{2,ads}$	K_{O_2,S_1}
	$site_{H_2O} + H_2O \leftrightarrow H_2O_{ads}$	K_{H_2O}
	$site_{H_2O} + H_2O \leftrightarrow OH^-{}_{ads} + H^+$	
	$site_{4\text{-}CP} + 4\text{-}CP \leftrightarrow 4\text{-}CP_{ads}$	$K_{4\text{-}CP,S_2}$
	$site_{4\text{-}CP} + 4\text{-}CC \leftrightarrow 4\text{-}CC_{ads}$	$K_{4\text{-}CC,S_2}$
	$site_{4\text{-}CP} + HQ \leftrightarrow HQ_{ads}$	K_{HQ,S_2}
	$site_{Y_{In}} + Y_{Y_{In}} \leftrightarrow Y_{Y_{In,\,ads}}$	K_{In}

S_1 = Site type 1; S_2 = Site type 2 with competitive adsorption.
$C_{o_2} \cong$ constant. $C_{H_2O_{ads}}$ and $C_{OH^-_{ads}} \cong$ constant.
X_i = organic degradation products of $4\text{-}CC_{ads}$.
X_j = organic degradation products of HQ_{ads}.
Y_{In} = inorganic radicals and species that compete to react with ·OH.
Adapted from Satuf et al. (2008).

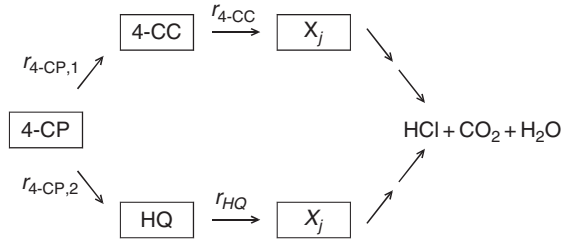

Figure 16 Reaction pathway suggested for the photocatalytic degradation of 4-chlorophenol in acidic medium.

Resorting to a balance of sites for competitive adsorption in sites type 2 and considering that the rate of electrons and holes can be expressed in terms of

$$R_g(x) = \frac{\bar{\Phi}}{a_V}\sum_{\lambda} e^a_\lambda(\underline{x}) = \frac{\bar{\Phi}}{a_V} e^a(\underline{x}) \tag{50}$$

the following reaction rates can be obtained:

$$\mathsf{R}_{4\text{-CP},1}(\underline{x},t) = \frac{\alpha_{2,1}C_{4\text{-CP}}(t)}{1+\alpha_3 C_{4\text{-CP}}(t)+\alpha_1' C_{4\text{-CC}}(t)+\alpha_2' C_{HQ}(t)} \times \left(-1+\sqrt{1+\frac{\alpha_1}{a_v}e^a(\underline{x})}\right) \tag{51}$$

$$\mathsf{R}_{4\text{-CP},2}(\underline{x},t) = \frac{\alpha_{2,2}C_{4\text{-CP}}(t)}{1+\alpha_3 C_{4\text{-CP}}(t)+\alpha_1' C_{4\text{-CC}}(t)+\alpha_2' C_{HQ}(t)} \times \left(-1+\sqrt{1+\frac{\alpha_1}{a_v}e^a(\underline{x})}\right) \tag{52}$$

$$\mathsf{R}_{4\text{-CC}}(\underline{x},t) = \frac{\alpha_4 C_{4\text{-CC}}(t)}{1+\alpha_3 C_{4\text{-CP}}(t)+\alpha_1' C_{4\text{-CC}}(t)+\alpha_2' C_{HQ}(t)} \times \left(-1+\sqrt{1+\frac{\alpha_1}{a_v}e^a(\underline{x})}\right) \tag{53}$$

$$\mathsf{R}_{HQ}(\underline{x},t) = \frac{\alpha_5 C_{HQ}(t)}{1+\alpha_3 C_{4\text{-CP}}(t)+\alpha_1' C_{4\text{-CC}}(t)+\alpha_2' C_{HQ}(t)} \times \left(-1+\sqrt{1+\frac{\alpha_1}{a_v}e^a(\underline{x})}\right) \tag{54}$$

In Equations (51)–(54), it must be noted that (i) $e^a(\underline{x}) = e^a[(\underline{x}), C_{cm}]$ to recall that the LVRPA is a strong function of the catalyst loading and (ii) there are eight lumped kinetic parameters that depend on intrinsic properties of the system according to

$$\alpha_1 = \frac{\bar{\Phi} 4 k_2}{k_4 k_3 C_{H_2O,ads} C_{O_{2,ads}}} \tag{55}$$

$$\alpha_{2,1} = \frac{k_5 k_4 k_3 C_{H_2O,ads} C_{O_{2,ads}} C_{site,4\text{-CP}} K_{4\text{-CP}}}{2k_2\left(\sum_{In} k_{In}'' C_{Y_{In,ads}}\right)} \tag{56}$$

$$\alpha_{2,2} = \frac{k_6 k_4 k_3 C_{H_2O,ads} C_{O_{2,ads}} C_{site,4\text{-CP}} K_{4\text{-CP}}}{2k_2\left(\sum_{In} k_{In}'' C_{Y_{In,ads}}\right)} \tag{57}$$

$$\alpha_3 = \frac{C_{\text{site,4-CP}}(k_5 + k_6)K_{\text{4-CP}} + K_{\text{4-CP}}}{\sum_{\text{In}} k''_{\text{In}} C_{\text{In,ads}}} \tag{58}$$

$$\alpha'_1 = \frac{C_{\text{site,4-CP}} k_7 K_{\text{4-CP}} + K_{\text{4-CC}}}{\sum_{\text{In}} k''_{\text{In}} C_{\text{In,ads}}} \tag{59}$$

$$\alpha'_2 = \frac{C_{\text{site,4-CP}} k_8 K_{\text{HQ}} + K_{\text{HQ}}}{\sum_{l} k''_{l} C_{l,\text{ads}}} \tag{60}$$

$$\alpha_4 = \frac{k_7 k_4 k_3 C_{\text{H}_2\text{O,ads}} C_{\text{O}_{2,\text{ads}}} C_{\text{site,4-CP},T} K_{\text{4-CC}}}{2k_2 \left(\sum_{\text{In}} k''_{\text{In}} C_{Y_{\text{In,ads}}} \right)} \tag{61}$$

$$\alpha_5 = \frac{k_8 k_4 k_3 C_{\text{H}_2\text{O,ads}} C_{\text{O}_{2,\text{ads}}} C_{\text{site,4-CP},T} K_{\text{HQ}}}{2k_2 \left(\sum_{\text{In}} k''_{\text{In}} C_{Y_{\text{In,ads}}} \right)} \tag{62}$$

4.2. Laboratory reactor: description and modeling

The laboratory reactor was designed with the same criteria described in Section 3.2. in order to simplify the modeling. The details are given in Table 9 and Figures 17, 18a, b, and 19. There are two important differences with respect to the previous case: (i) both windows are mobile in the direction of the reactor length and the displacement is made with a single consolidate unit of the window and the irradiation system to keep the irradiation rate on each surface constant and (ii) interposed between the reactors windows made of borosilicate glass and the position built to insert the shutters (to start the reaction at a desired time) and the filters (to attenuate the incoming radiation when needed), there are two fixed circular plates made of ground glass to produce diffuse irradiation on each surface of radiation entrance. Diffuse incoming radiation means azimuthal symmetry in both boundary conditions (Figure 18a). With these arrangements, three different reactor lengths were selected (0.5, 1, and 5 cm) to study the effect of the optical thickness (catalyst concentration plus radiation path) allowing for a two orders of magnitude change on the variable. Similarly, with the neutral density filters the incoming radiation was changed in three levels: 100, 67, and 30%. For more details about the experimental setup and the operating conditions the reader is referred to Satuf et al. (2007a, b, 2008).

Table 9 Laboratory and pilot scale reactor description and operating conditions

Item	Specification/Dimensions	
	Laboratory reactor	Pilot scale reactor
Type	Flat plate. Batch, with a recycle. Two circular windows made of borosilicate glass	Flat plate with recycle. Irradiated from one wall with two tubular lamps and parabolic reflectors
Reactor volume	Photoreactor: V_R = from 29.03 to 290.29 cm^3 Total: $V_T = 1{,}000\ cm^3$	Photoreactor: $V_R = 734.4\ cm^3$ Total system volume: $V_T = 5{,}000\ cm^3$
Dimensions	Two sides. D(inner) = 8.6 cm L_R = Variable from 0.5 to 5 cm	Length: $Z_R = 34.0$ cm Width: $Y_R = 18.0$ cm Thickness: $X_R = 1.2$ cm
Lamps	Four in each side (total 8)	Two. On the front
Pilot reactor: Actinic: without built-in reflectors	Philips: TL 4W/08 Black Light UVA Output power: 4 W each Arc length: 13.6 cm $R_L = 0.8$ cm	Philips: TLK40/09 Actinic UVA Output power: 40 W each $Z_L = 60$ cm $R_L = 3.8$ cm
Wavelength	300–400 nm (peak: 350 nm)	310–400 nm (peak: 350 nm)
Reflectors	None	Two parabolic cylinders. Made of aluminum, specularly finished

Table 9 (*Continued*)

Item	Specification/Dimensions	
	Laboratory reactor	Pilot scale reactor
Incident radiation at the wall	Measured by actinometry (potassium ferrioxalate) 100% (without filters): 7.55×10^{-9} Einstein cm^{-2} s^{-1} (at each window)	Calculated with a superficial emission model
Operation		
Flow rate	Recirculation: 6,000 cm^3 min^{-1}	Recirculation: 6,000 cm^3 min^{-1}
Temperature	20°C	20°C
Pressure	1 atm.	1 atm.
Catalyst concentration	0.05, 0.1, 0.5, and 1.0×10^{-3} g cm^{-3}	0.05, 0.1, 0.5. and 1.0×10^{-3} g cm^{-3}
Initial 4-CP concentration	1.5×10^{-7} mol cm^{-3}	1.5×10^{-7} mol cm^{-3}
Initial pH	2.5	2.5

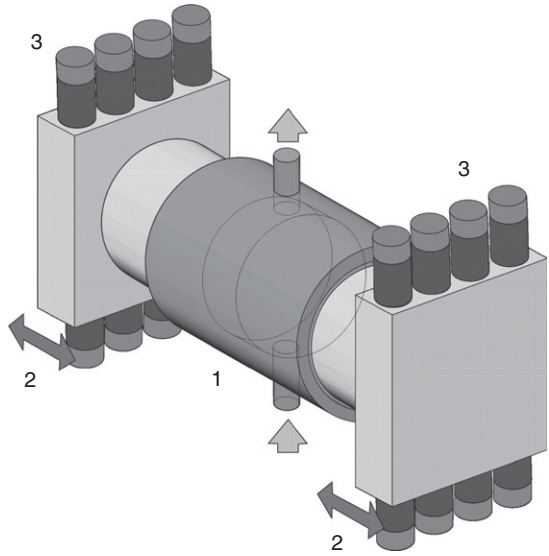

Figure 17 Schematic representation of the photocatalytic reactor. Keys: (1) reactor, (2) mobile windows system, (3) radiation emitting system.

Employing a high recirculating flow rate in this small laboratory reactor, the following assumptions can be used: (i) there is a differential conversion per pass in the reactor, (ii) the system is perfectly stirred, (iii) there are no mass transport limitations. Also, it can be assumed that (iv) the chemical reaction occurs only at the solid–liquid interface (Minero et al., 1992) and (v) direct photolysis is neglected (Satuf et al., 2007a). As a result, the mass balance for the species i in the system takes the following form (Cassano and Alfano, 2000):

$$\varepsilon_L \frac{\mathrm{d}C_i(t)}{\mathrm{d}t}\bigg|_{Tk} = \frac{V_R}{V_T} a_v \langle v_i \mathsf{R}(\underline{\mathrm{x}}, t)\rangle_{A_R} \quad i = \text{4-CP, 4-CC, HQ} \tag{63}$$

where ε_L is the liquid hold-up ($\varepsilon_L \cong 1$), C_i is the molar concentration of the component i and $\langle R(\underline{\mathrm{x}}, t)\rangle_{A_R}$ is the superficial reaction rate averaged over the catalytic reaction area.

The primary oxidation products of 4-CP are 4-CC, HQ, and benzoquinone (BQ) (Theurich et al., 1996). Under the experimental conditions employed in our work, at pH 2.5, the oxidation via 4-CC represents the main pathway for the degradation of 4-CP. In second place appears the formation of HQ. Because of the low concentrations of BQ found during the experiments, this intermediate product is not considered in the kinetic model. Then, the

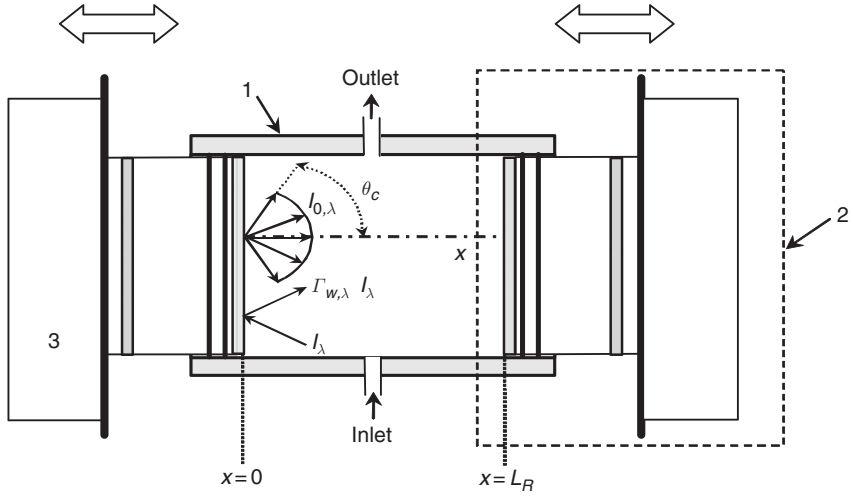

(a)

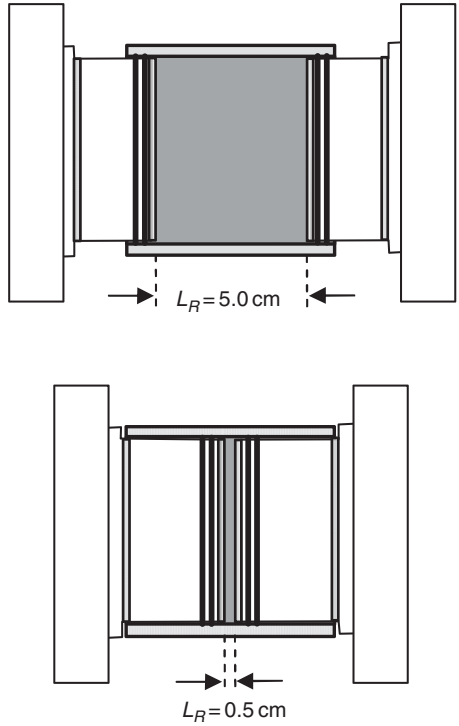

(b)

Figure 18 (a) Diagram of mobile windows mechanism. (b) Sketch of maximum and minimum reactor length.

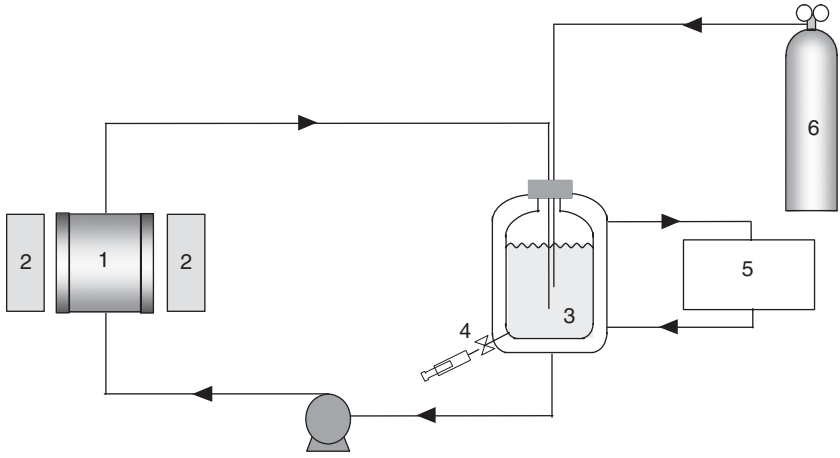

Figure 19 Schematic representation of the experimental setup. Keys: (1) reactor, (2) radiation emitting system, (3) tank, (4) sampling valve, (5) thermostatic bath, (6) oxygen supply, (7) pump.

mass balances for 4-CP, 4-CC, and HQ, with the corresponding initial conditions, are

$$\varepsilon_L \frac{dC_{4\text{-CP}}(t)}{dt} = -\frac{V_R}{V_T} a_v \left\{ \left\langle \mathsf{R}_{4\text{-CP},1}(\underline{x}, t) \right\rangle_{A_R} + \left\langle \mathsf{R}_{4\text{-CP},2}(\underline{x}, t) \right\rangle_{A_R} \right\} \times C_{4\text{-CP}}(t = 0) = C_{4\text{-CP},0} \tag{64}$$

$$\varepsilon_L \frac{dC_{4\text{-CC}}(t)}{dt} = \frac{V_R}{V_T} a_v \left\{ \left\langle \mathsf{R}_{4\text{-CP},1}(\underline{x}, t) \right\rangle_{A_R} - \left\langle \mathsf{R}_{4\text{-CC}}(\underline{x}, t) \right\rangle_{A_R} \right\} \times C_{4\text{-CC}}(t = 0) = 0 \tag{65}$$

$$\varepsilon_L \frac{dC_{\text{HQ}}(t)}{dt} = \frac{V_R}{V_T} a_v \left\{ \left\langle \mathsf{R}_{4\text{-CP},2}(\underline{x}, t) \right\rangle_{A_R} - \left\langle \mathsf{R}_{\text{HQ}}(\underline{x}, t) \right\rangle_{A_R} \right\} \times C_{\text{HQ}}(t = 0) = 0 \tag{66}$$

As shown in Equations (51)–(54) and Figure 16, two parallel reaction pathways are postulated for the degradation of 4-CP: $\mathsf{R}_{4\text{-CP},1}$ represents the degradation rate to give 4-CC, whereas $\mathsf{R}_{4\text{-CP},2}$ is the rate that leads to the formation of HQ. $\mathsf{R}_{4\text{-CC}}$ and R_{HQ} denote the degradation rates of 4-CC and HQ.

Equations (51)–(54) indicate the need for calculating e^a_λ and $\Sigma_\lambda e^a_\lambda$.

The evaluation of the LVRPA inside the reactor was achieved by solving the RTE for the heterogeneous system. The radiation model considers that

(Figure 18a) (i) the main changes in the spatial distribution occur along the x coordinate axis due to the significant extinction produced by the TiO_2 catalyst particles; thus, a one-dimensional (x in space) model can be applied and (ii) the arrangement of the four UV lamps and the ground glass plates at the external side of the reactor windows ensure the arrival of diffuse radiation with azimuthal symmetry; consequently, radiation intensity in the medium is independent of the azimuthal angle and a one-directional (θ in direction) radiation model can be assumed. Then, a one-dimensional, one-directional radiation transport model is applied (Alfano et al., 1995; Cassano et al., 1995):

$$\mu \frac{\partial I_\lambda(x,\mu)}{\partial x} + \beta_\lambda I_\lambda(x,\mu) = \frac{\sigma_\lambda}{2} \int_{\mu'=-1}^{1} I_\lambda(x,\mu')\, p(\mu,\mu') \mathrm{d}\mu' \tag{67}$$

In Equation (67) β_λ is the extinction coefficient, μ the direction cosine of the ray for which the RTE is written, μ' the cosine of an arbitrary ray before scattering, and "p" the phase function for scattering.

The Henyey and Greenstein phase function ($p_{HG,\lambda}$) was adopted to model the radiation scattering of the TiO_2 suspensions (Siegel and Howell, 2002):

$$p_{HG,\lambda}(\mu_0) = \frac{1 - {g_\lambda}^2}{(1 + {g_\lambda}^2 - 2 g_\lambda \mu_0)^{3/2}} \tag{68}$$

It is worth noting that $p_{HG,\lambda}$ is determined by a single parameter, the dimensionless asymmetry factor (g_λ), that varies from isotropic ($g_\lambda = 0$) to a narrow forward peak ($g_\lambda = 1$) or to a narrow backward peak ($g_\lambda = -1$); this parameter can be estimated employing the method described in Satuf et al. (2005).

Equation (67) must be solved with the appropriate boundary conditions in terms of the radiation intensity. At $x = 0$, radiation intensities are the result of the transmitted portion of the radiation arriving to the reactor glass plate and the reflected portion of the radiation coming from the aqueous suspension (Figure 18a).

It should be also noted that (i) the radiation coming from the lamps arrives in a diffuse way at the external side of the glass window. The angular directions of the intensities entering the suspension ($I_{0,\lambda}$) are comprised between 0 and the critical angle θ_c; this fact can be explained taking into account that radiation must cross two interfaces: air-glass and glass suspension and (ii) the intensities coming from the reacting medium undergo multiple specular reflections at the reactor window. For this case, a global reflection coefficient ($\Gamma_{W,\lambda}$) can be defined; it represents the reflected fraction of the radiation that goes back to the suspension.

A similar analysis can be applied for the boundary condition at $x = L_R$:

$$I_\lambda(0,\mu) = I_{0,\lambda} + \Gamma_{W,\lambda}(-\mu) I_\lambda(0,-\mu) \quad 1 \geq \mu \geq \mu_c \tag{69a}$$

$$I_\lambda(0,\mu) = \Gamma_{W,\lambda}(-\mu) I_\lambda(0,-\mu) \quad \mu_c \geq \mu \geq 0 \tag{69b}$$

$$I_\lambda(L_R,-\mu) = I_{L_R,\lambda} + \Gamma_{W,\lambda}(\mu) I_\lambda(L_R,\mu) \quad 1 \geq \mu \geq \mu_c \tag{69c}$$

$$I_\lambda(L_R,-\mu) = \Gamma_{W,\lambda}(\mu) I_\lambda(L_R,\mu) \quad \mu_c > \mu \geq 0 \tag{69d}$$

Here μ_c is the cosine of the critical angle θ_c. More details on the one-dimensional, one-directional radiation model can be found in Satuf et al. (2007a).

To solve Equations (67)–(69), the Discrete Ordinate Method was applied (Duderstadt and Martin, 1979). From the solution of the RTE, the monochromatic radiation intensity at each point and each direction inside the reactor can be obtained. Considering constant optical properties of the catalyst and steady radiation supply by the emitting system, the radiation field can be considered independent of time.

The LVRPA for polychromatic radiation is calculated from the values of the monochromatic radiation intensity as

$$e^a(x) = 2\pi \int_\lambda \kappa_\lambda \int_{\mu=-1}^{1} I_\lambda(x,\mu) \mathrm{d}\mu \mathrm{d}\lambda \tag{70}$$

Figure 20 shows LVRPA profiles for different TiO_2 concentrations and for the three values of the reactor lengths employed in the experimental runs. In Figure 20a, the strongest variations of LVRPA are observed for the highest catalyst loading ($C_m \geq 0.5 \times 10^{-3}$ g cm^{-3}) and for the largest reactor ($L_R = 5.0$ cm). Smoother profiles are obtained as long as the catalyst loading and the reactor length decrease.

4.3. Kinetic results

A nonlinear, multiparameter regression procedure (Levenberg–Marquardt method) was applied to estimate the kinetic parameters involved in Equations (51)–(54). The experimental concentrations of the pollutant (4-CP) and of the main intermediate species (4-CC and HQ) at different reaction times were compared with model predictions. Under the operating conditions of the experimental runs, it was found that the terms $\alpha_3 C_{4\text{-CP}}(t)$, $\alpha_1' C_{4\text{-CC}}(t)$, and $\alpha_2' C_{\text{HQ}}(t)$ were much lower than 1. As a result, the final expressions employed for the regression of the kinetic parameters are the following:

$$\mathsf{R}_{4\text{-CP},1}(x,t) = \alpha_{2,1} C_{4\text{-CP}}(t) \left(-1 + \sqrt{1 + \frac{\alpha_1}{a_v} e^a(x)} \right) \tag{71}$$

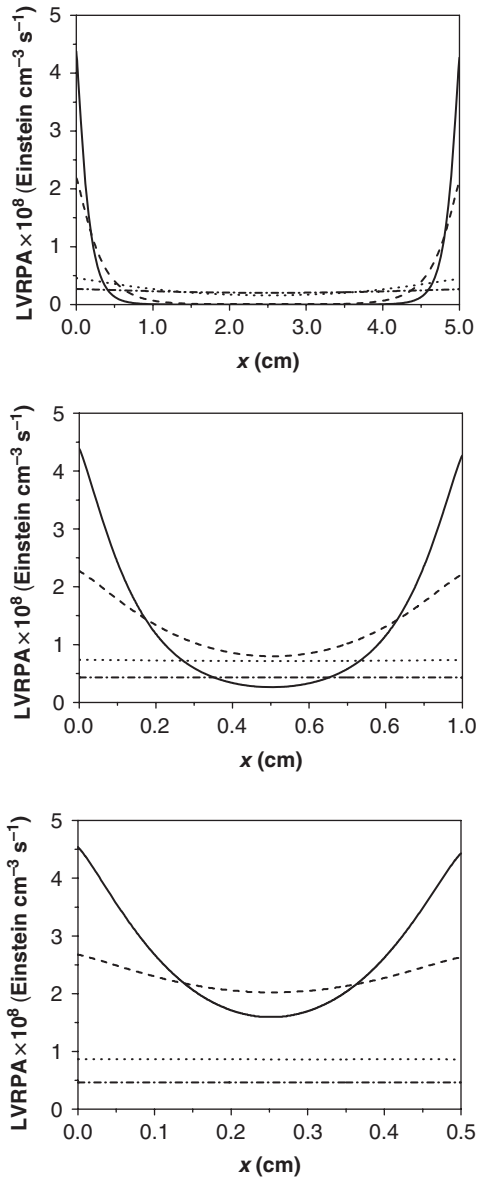

Figure 20 LVRPA profiles for different catalyst concentrations and different reactor lengths. (———): $C_m = 1.0 \times 10^{-3}$ g cm^{-3}; (– – – –): $C_m = 0.5 \times 10^{-3}$ g cm^{-3}; (· · · ·): $C_m = 0.1 \times 10^{-3}$ g cm^{-3}; (– · – ·): $C_m = 0.05 \times 10^{-3}$ g cm^{-3}. (a) $L_R = 5.0$ cm, (b) $L_R = 1.0$ cm, (c) $L_R = 0.5$ cm.

$$R_{4\text{-}CP,2}(x,t) = \alpha_{2,2} C_{4\text{-}CP}(t)\left(-1+\sqrt{1+\frac{\alpha_1}{a_v}e^a(x)}\right) \tag{72}$$

$$R_{4\text{-}CC}(x,t) = \alpha_4 C_{4\text{-}CC}(t)\left(-1+\sqrt{1+\frac{\alpha_1}{a_v}e^a(x)}\right) \tag{73}$$

$$R_{HQ}(x,t) = \alpha_5 C_{HQ}(t)\left(-1+\sqrt{1+\frac{\alpha_1}{a_v}e^a(x)}\right) \tag{74}$$

Table 10 provides the values of the five kinetic parameters, with the corresponding 95% confidence interval. Note that $\alpha_{2,1} \cong 5\alpha_{2,2}$, showing that the 4-CP degradation via 4-CC is favored, being 4-CC the most abundant primary intermediate (Satuf et al., 2008).

Figures 21a, b show the 4-CP, 4-CC, and HQ concentrations derived from inserting the estimated parameters in the kinetic model and a comparison with the experimental data under different operating conditions. Symbols correspond to experimental data and solid lines to model predictions calculated with Equations (64)–(66) and Equations (71)–(74). For these experimental runs, the RMSE was less than 14.4%. These experimental 4-CC and HQ concentrations are in agreement with the proposed kinetic mechanism of parallel formation of the intermediate species (Figure 16), and also with the "series–parallel" kinetic model reported by Salaices et al. (2004) to describe the photocatalytic conversion of phenol in a slurry reactor under various operating conditions.

The term $\psi = \left(-1+\sqrt{1+\frac{\alpha_1}{a_v}e^a(x)}\right)$ in Equations (71)–(74) can be used to study the dependence of reaction kinetics on the photon absorption rate. The following limiting cases may be readily obtained: (i) for sufficiently high values of e^a, it holds that $\frac{\alpha_1}{a_v}e^a(x) \gg 1$ and $\sqrt{1+\frac{\alpha_1}{a_v}e^a(x)} \approx \sqrt{\frac{\alpha_1}{a_v}e^a(x)}$; additionally, if $\sqrt{\frac{\alpha_1}{a_v}e^a(x)} \gg -1$, then $\psi \approx \sqrt{\frac{\alpha_1}{a_v}e^a(x)}$. Therefore, under high

Table 10 Kinetic parameters of 4-CP decomposition

Parameter	Value	Confidence interval (95%)	Units
α_1	1.09×10^{11}	$\pm 0.07 \times 10^{11}$	s cm^2 Einstein^{-1}
$\alpha_{2,1}$	9.43×10^{-6}	$\pm 0.26 \times 10^{-6}$	cm s^{-1}
$\alpha_{2,2}$	2.18×10^{-6}	$\pm 0.46 \times 10^{-6}$	cm s^{-1}
α_4	1.29×10^{-5}	$\pm 0.08 \times 10^{-5}$	cm s^{-1}
α_5	9.21×10^{-6}	$\pm 0.96 \times 10^{-6}$	cm s^{-1}

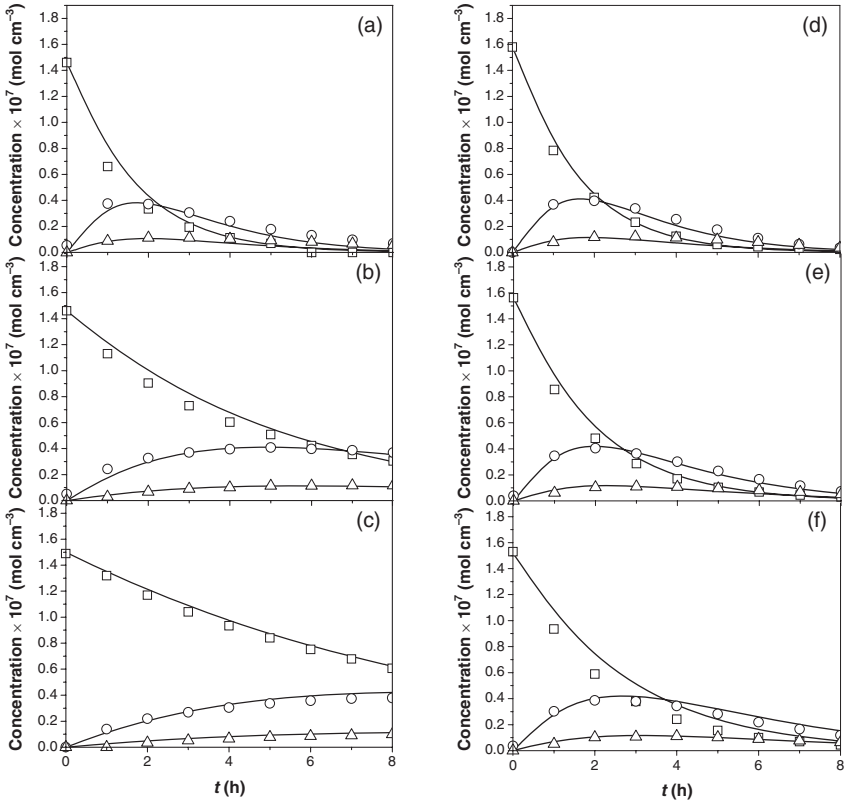

Figure 21 Experimental and predicted concentrations of 4-CP, 4-CC, and HQ versus time. Left: $L_R = 1.0$ cm, $E_L = 100\%$ and different C_m. Experimental data: □: 4-CP; ○: 4-CC; △: HQ. Model results: solid lines. (a) $C_m = 1.0 \times 10^{-3}$ g cm^{-3}; (b) $C_m = 0.1 \times 10^{-3}$ g cm^{-3}; (c) $C_m = 0.05 \times 10^{-3}$ g cm^{-3}. Right: $C_m = 0.5 \times 10^{-3}$ g cm^{-3}, $E_L = 100\%$ and different L_R. Experimental data: □: 4-CP; ○: 4-CC; △: HQ. Model results: solid lines. (d) $L_R = 5.0$ cm; (e) $L_R = 1.0$ cm; (f) $L_R = 0.5$ cm.

values of e^a, the reaction rate is proportional to the square root of the LVRPA. (ii) For rather low values of e^a: $\frac{\alpha_1}{a_v} e^a(x) << 1$; thus, from a Taylor series expansion, it can be shown that $\sqrt{1 + \frac{\alpha_1}{a_v} e^a(x)} \approx 1 + \frac{1\alpha_1}{2a_v} e^a(x)$ (Alfano et al., 1997). Hence, for low values of e^a, $\psi \approx \frac{1\alpha_1}{2a_v} e^a(x)$ and the reaction rate has a linear dependence with respect to the LVRPA. Table 11 describes the numerical results obtained for two laboratory reactor lengths and two catalyst concentrations: (i) for $L_R = 5.0$ cm, $C_m = 1.0 \times 10^{-3}$ g cm^{-3}, and $x = 0$ (at the reactor window), the dependence of the reaction rate is nearly proportional to the square root of the LVRPA, whereas at $x = L_R/2$ (in the center of the reactor) the same dependence is linear. (ii) For $L_R = 0.5$ cm,

Table 11 Dependence of the reaction rate on the photon absorption rate

L_R (cm)	C_m ($\times 10^3$ g cm^{-3})	X	$\frac{\alpha_1}{a_v} e^a(x)$	$\sqrt{\frac{\alpha_1}{a_v} e^a(x)}$
5	1.0	0	49.7	7.05
5	1.0	$L_R/2$	1.15×10^{-4}	1.07×10^{-2}
0.5	0.05	0	105.6	10.3
0.5	0.05	$L_R/2$	105.6	10.3

$C_m = 0.05 \times 10^{-3}$ g cm^{-3}, the reaction rate is proportional to the square root of the LVRPA throughout the reaction space. Consequently, in a photocatalytic slurry reactor, where low, intermediate, and high photon absorption rates can coexist, the complete reaction rate equation must be used.

4.4. Pilot scale reactor

Figures 22a, b provides a schematic representation of the pilot scale reactor. Essentially it is a rectangular parallelepiped limited by two parallel windows made of borosilicate glass and operated as a slurry reactor inside the loop of a batch recycling system. Irradiation of one of the reactor faces is obtained using two tubular lamps that were placed along the focal axis of two parabolic reflectors made of specularly finished aluminum (Brandi et al., 1996, 1999, 2002). The specific information concerning the experimental device is presented in Table 9, and more details can be found in Satuf et al. (2007b).

4.5. Reactor model

The mass balance in the reactor is derived under the following assumptions: (i) unsteady state operation, (ii) convective laminar Newtonian flow in the axial direction z (the Reynolds number is below the transition regime), (iii) diffusion in the z direction is negligible with respect to convection, (iv) symmetry in the y direction (the lamp length is much larger than the reactor width), and (v) constant physical properties. The local mass balance for a species i in the reactor and the corresponding initial and boundary conditions are

$$\frac{\partial C_{i,R}}{\partial t} + v_z \frac{\partial C_{i,R}}{\partial z} - D_i \frac{\partial^2 C_{i,R}}{\partial x^2} - \mathsf{R}_i = 0; \quad i = \text{4-CP, 4-CC, HQ} \tag{75}$$

$$C_{i,R}(x, z, t = 0) = C_{i,0} \tag{76}$$

$$C_{i,R}(x, z = 0, t) = C^o_{i,\mathrm{Tk}}(t) \tag{77}$$

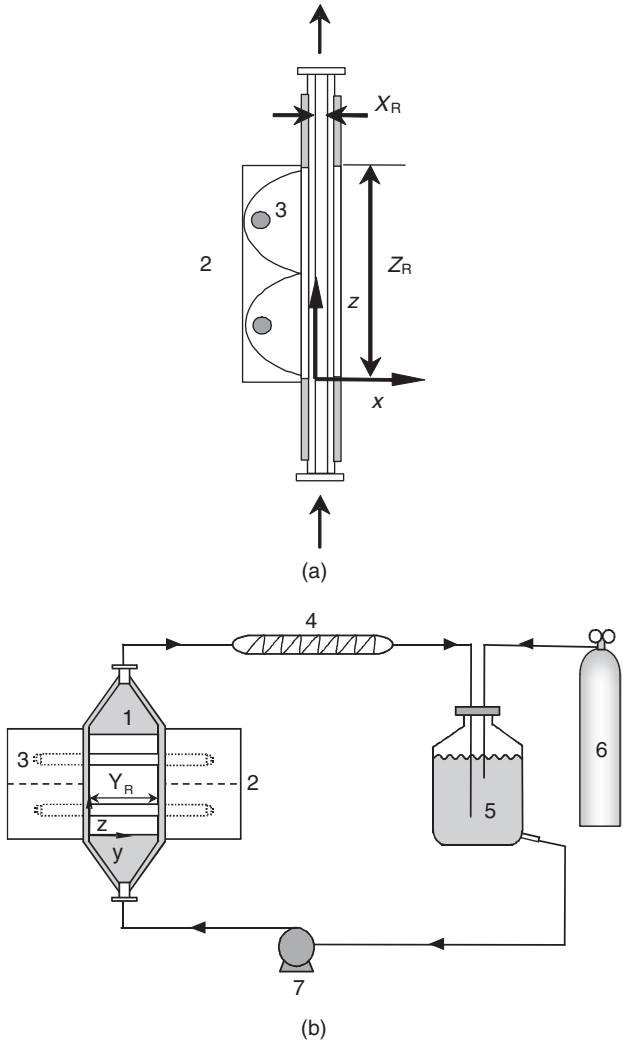

Figure 22 Schematic representation of the pilot scale experimental device. (a) Lateral view of the reactor. (b) Setup. Keys: (1) front view of the reactor, (2) reflectors, (3) lamps, (4) heat exchanger, (5) tank, (6) oxygen supply, (7) pump.

$$\left.\frac{\partial C_{i,R}}{\partial x}\right|_{x=0} = 0 \qquad \left.\frac{\partial C_{i,R}}{\partial x}\right|_{x=X_R} = 0 \tag{78}$$

$C_{i,0}$ is the initial concentration and $C^{o}_{i,\mathrm{Tk}}$ is the exit concentration from the tank.

The reaction rate R_i in Equation (75) for the species 4-CP, 4-CC, and HQ was replaced by the Equations (71)–(74) with the kinetic parameters reported in Table 10.

The concentrations of 4-CP, 4-CC, and HQ as a function of x, z, and t can be obtained solving Equations (75)–(78). The average exit concentration from the reactor at a given time t is given by

$$\left\langle C_{i,R}(x, z = Z_R, t)\right\rangle_{A_R} = \frac{\displaystyle\int_{x=0}^{x=X_R} C_{i,R}(x, z = Z_R, t) v_z(x)\mathrm{d}x}{\displaystyle\int_{x=0}^{x=X_R} v_z(x)\mathrm{d}x} = C^i_{i,\mathrm{Tk}}(t) \tag{79}$$

Equation (79) gives the inlet condition for the mass balance in the tank, $C^i_{i,\mathrm{Tk}}(t)$.

Considering that the tank operates under unsteady state and well-stirred conditions, the mass balance and the initial condition for a species i yields

$$\varepsilon_L \frac{\mathrm{d}C_i(t)}{\mathrm{d}t}\bigg|_{\mathrm{Tk}} = \frac{1}{\tau_{\mathrm{Tk}}}\left[C^i_{i,\mathrm{Tk}}(t) - C^o_{i,\mathrm{Tk}}(t)\right]; \quad i = \text{4-CP, 4-CC, HQ} \tag{80}$$

$$C^i_{i,\mathrm{Tk}}(t = 0) = C_{i,0} \tag{81}$$

where τ_{Tk} is the mean residence time in the tank.

4.6. Radiation model

The existence of the LVRPA in the reaction rate expression (Equation 75) makes necessary the solution of the RTE in the pilot scale reactor. As explained before, the lamps length is significantly larger than the reactor width Y_R, thus uniformity of radiation is considered along the y direction. Therefore, a two-dimensional (x, z) model for the spatial variations of the radiation field was adopted. The angular distribution of radiation was modeled with the spherical coordinates (θ, ϕ). The RTE for a two-dimensional, two-directional model is (Brandi et al., 1996, 1999),

$$\begin{aligned}\mu\frac{\partial I_\lambda(x,\ z,\ \underline{\Omega})}{\partial x} + \eta\frac{\partial I_\lambda(x,\ z,\ \underline{\Omega})}{\partial z} + \beta_\lambda I_\lambda(x, z, \underline{\Omega}) \\ = \frac{\sigma_\lambda}{4\pi}\int_{\Omega'=4\pi} I_\lambda(x, z, \underline{\Omega}')p(\underline{\Omega}' \to \underline{\Omega})\mathrm{d}\Omega'\end{aligned} \tag{82}$$

where $\mu = \cos\phi \sin\theta$ and $\eta = \sin\phi \sin\theta$. The boundary conditions are

$$I_\lambda(x=0,z,\underline{\Omega}=\underline{\Omega}^i)=\chi(\text{properties corresponding to the emitting system and the reactor wall})$$

$$I_\lambda(x=X_R,z,\underline{\Omega}=\underline{\Omega}^i)=\chi(\text{properties corresponding to the reactor wall})$$

$$I_\lambda(x,z=0,\underline{\Omega}=\underline{\Omega}^i)=0;I_\lambda(x,z=Z_R,\underline{\Omega}=\underline{\Omega}^i)=0 \tag{83}$$

where $\underline{\Omega}^i$ represents the directions of radiation intensity entering the reactor.

The radiation flux at the wall of radiation entrance (Figure 22) was determined by actinometric measurements (Zalazar et al., 2005). Additionally, the boundary condition for this irradiated wall ($x=0$) was obtained using a lamp model with superficial, diffuse emission (Cassano et al., 1995) considering: (i) direct radiation from the two lamps and (ii) specularly reflected radiation from the reflectors (Brandi et al., 1996). Note that the boundary conditions at the irradiated and opposite walls consider the effect of reflection and refraction at the air–glass and glass–liquid interfaces, as well as the radiation absorption by the glass window at low wavelengths (the details were shown for the laboratory reactor). The radiation model also assumes that no radiation arrives from the top and bottom reactor walls (x–y plane at $z=0$ and $z=Z_R$).

The discrete ordinate method (Duderstadt and Martin, 1979) was employed to solve the RTE (Equations 82 and 83). Afterward, the LVRPA was obtained according to

$$e^a(x,z)=\int_\lambda \kappa_\lambda \int_\Omega I_\lambda(x,z,\underline{\Omega})\mathrm{d}\Omega\mathrm{d}\lambda \tag{84}$$

where the limit Ω indicates all radiation arrival directions at a given point (x, z).

4.7. Validation

Figure 23a shows the predicted and experimental concentrations versus time of 4-CP, 4-CC, and HQ for a catalyst mass concentration of 0.5×10^{-3} g cm^{-3}. As can be observed, the 4-CP concentration decreases throughout the experimental run following a first-order kinetics and the pollutant is completely degraded after 6 h of irradiation. This figure also shows the formation and destruction of 4-CC and HQ, with a maximum at approximately 1h. Then, these two main intermediate species decrease gradually until they almost disappear at the end of the run. The changes in the 4-CC and HQ concentrations are consistent with the proposed kinetic mechanism reported in Section 4.3, and with the "series–parallel" kinetic model

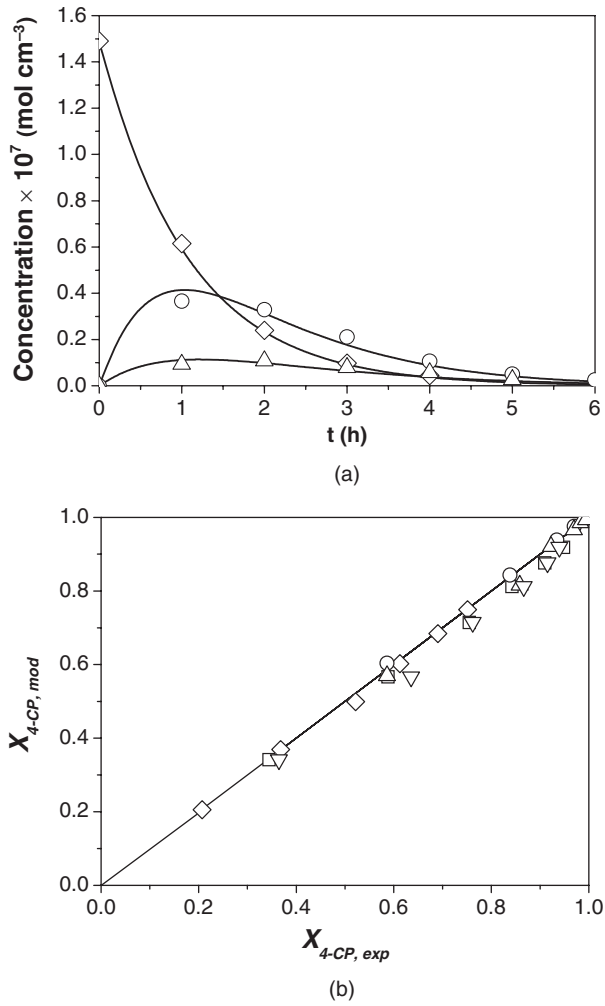

Figure 23 (a) Experimental and predicted concentrations versus time for $C_m = 0.5 \times 10^{-3}$ g cm^{-3}. Solid line: model predictions. Symbols: experimental data. ◇: 4-CP, ○: 4-CC, △: HQ. (b) Experimental versus predicted conversions of 4-CP. Symbols correspond to different runs: ◇: $C_{4\text{-CP},0} = 1.4 \times 10^{-7}$ mol cm^{-3} and $C_m = 0.05 \times 10^{-3}$ g cm^{-3}, □: $C_{4\text{-CP},0} = 1.4 \times 10^{-7}$ mol cm^{-3} and $C_m = 0.1 \times 10^{-3}$ g cm^{-3}, ○: $C_{4\text{-CP},0} = 1.4 \times 10^{-7}$ mol cm^{-3} and $C_m = 0.5 \times 10^{-3}$ g cm^{-3}, △: $C_{4\text{-CP},0} = 1.4 \times 10^{-7}$ mol cm^{-3} and $C_m = 1.0 \times 10^{-3}$ g cm^{-3}, ▽: $C_{4\text{-CP},0} = 0.7 \times 10^{-7}$ mol cm^{-3} and $C_m = 0.1 \times 10^{-3}$ g cm^{-3}.

proposed by Salaices et al. (2004) for the photocatalytic degradation of phenolic compounds in an annular slurry recycling reactor. The total organic carbon (TOC) evolution has been also reported by Satuf et al. (2008) for a typical experimental run (results not shown here). The TOC

concentration decreases slowly, remaining a significant amount of organic carbon at the end of the run. This fact can be explained by the generation of aliphatic compounds, mainly aldehydes and carboxylic acids, not detected by high performance liquid chromatography analysis.

The quality of the scaling-up procedure can be seen when experimental and predicted 4-CP conversions for the pilot scale reactor are compared in Figure 23b. The symbols correspond to the 4-CP conversions obtained at different reaction times for all the experimental runs performed in this reactor. Predicted concentrations of 4-CP and 4-CC compared with experimental results show an RMSE lower than 9.91%. HQ was not included in the computation of the RMSE due to the low concentrations obtained during the experiments.

5. CONCLUSIONS

To some extent, the conclusions are very simple. These three examples, with three very different applications, corroborate the statement made in Section 1.

We have been able to scale-up results obtained in small-scale laboratory reactors results to reactors of completely different sizes, shapes, configurations, and operating conditions. The method has been illustrated with three typical and distinct applications: (i) a wall reactor, with an immobilized catalyst in a nonparticipating gaseous medium, (ii) a homogeneous photochemical process in a continuous flow, annular reactor operated in an aqueous medium, and (iii) a slurry reactor, working in a heterogeneous, participating medium, employing a photocatalyst with strong absorption and scattering properties. In all cases, the results have shown to be very satisfactory.

Four necessary conditions must be fulfilled in order to be able to move from laboratory experiments to larger scale reactor without employing (a) experimentally adjustable parameters and (b) costly successive physical changes of reactor sizes.

These conditions are (i) it is needed to have a validated kinetic scheme (a detailed mechanism or a precise empirical representation), (ii) it is needed to have a validated, intrinsic reaction kinetic expression as a function of position and time $[\mathsf{R}(x,t)]$, (iii) it is needed to use in both reactors the same spectral radiation output power distribution [λ for monochromatic radiation and $f(\lambda)$ for the polychromatic cases], and (iv) it is needed to apply and correctly solve a rigorous mathematical model to both the laboratory and the large-scale reactor.

In other words, the scale-up of photochemical or photocatalytic reactors not only needs a good chemical knowledge of the reaction (which is indispensable), but the application of the fundamental principles of chemical reaction engineering that, in addition, almost always call for a decision to use without aversion, physics, mathematics, and numerical methods as well.

ACKNOWLEDGMENTS

The authors are grateful to Universidad Nacional del Litoral (UNL), Consejo Nacional de Investigaciones Científicas y Técnicas (CONICET), and Agencia Nacional de Promoción Científica y Tecnológica (ANPCyT) for financial support. We also thank Tec. Antonio C. Negro and Eng. Gerardo Rintoul for their participation in some parts of the experimental work and Eng. Claudia Romani for her technical assistance.

Table 7 has been reproduced from Helv. Chim. Acta; Reference: Labas et al., 2002, "Scaling-Up of a Photoreactor for Formic Acid Degradation Employing Hydrogen Peroxide and UV Radiation", Table; Copyright 2002, with permission from Helv. Chim. Acta.

Table 10 has been reproduced from Appl. Catal. B: Environ.; Reference: Satuf et al., 2008, Photocatalytic degradation of 4-chlorophenol: A kinetic Study, Table 4; Copyright 2008, with permission from Elsevier Ltd.

Table 11 has been reproduced from Appl. Catal. B: Environ.; Reference: Satuf et al., 2008, Photocatalytic degradation of 4-chlorophenol: A kinetic Study, Table 5; Copyright 2008, with permission from Elsevier Ltd.

Figures 1 and 2 have been reproduced from Int. J. Chem. React. Eng.; Reference: Alfano, O.M., Cassano, A.E., 2008, Photoreactor modeling. Applications to advanced oxidation processes, figures 1 and 2, Copyright 2008, with permission from The Berkeley Electronic Press.

Figures 3–8 and 10 have been reproduced from Chem. Eng. Sci.; Reference: Imoberdorf et al., 2007, Scaling-up from first principles of a photocatalytic reactor for air pollution remediation, figures 1–3, 5, 7, 8, and 10, Copyright 2006, with permission from Elsevier Ltd.

Figures 11–15 have been reproduced from Helv. Chim. Acta; Reference: Labas et al., 2002, Scaling-up of a photoreactor for formic acid degradation employing hydrogen peroxide and UV radiation, figures 1–7, Copyright 2002, with permission from Helv. Chim. Acta.

Figures 16–21 have been reproduced from Appl. Catal. B: Environ.; Reference: Satuf et al., 2008, Photocatalytic degradation of 4-chlorophenol: A kinetic Study, figures 1–4, 6, 10 and 11, Copyright 2008, with permission from Elsevier Ltd.

Figures 22 and 23 have been reproduced from Catal. Today, Vol. 129; Reference: Satuf et al., 2007b, Scaling up of slurry reactors for photocatalytic degradation of 4-chlorophenol, figures 3 and 4, Copyright 2007, with permission from Elsevier Ltd.

NOTATION

A	area (cm^2)
a_V	catalytic surface area per unit suspension volume (cm^{-1})
C	molar concentration (mol cm^{-3})
Cm	catalyst mass concentration (g cm^{-3})

c speed of light (m s^{-1})
D_i diffusion coefficient of species i in the mixture (cm^2 s^{-1})
E radiative energy (J)
e thickness (cm)
e^a local volumetric rate of photon absorption (Einstein cm^{-3} s^{-1})
$e^{a,s}$ local superficial rate of photon absorption (Einstein cm^{-2} s^{-1})
G incident radiation (Einstein cm^{-2} s^{-1})
g asymmetry factor (dimensionless)
I radiation intensity (Einstein cm^{-2} sr^{-1} s^{-1})
K equilibrium constant (m^3 mg^{-1})
L length (cm)
n number of times that a radiation beam has been attenuated by a glass or a film (dimensionless)
$\underline{\mathrm{n}}$ unit normal vector (dimensionless)
P emission power (Einstein s^{-1})
p phase function (dimensionless)
Q volumetric flow rate (cm^3 s^{-1})
q net radiative flux (Einstein cm^{-2} s^{-1})
R radius (cm)
R reaction rate (mol cm^{-3} s^{-1})
r radial coordinate (cm); also, molar ratio C_P/C_F (dimensionless)
s linear coordinate along the direction $\underline{\Omega}$ (cm)
t time (s)
V volume (cm^3)
v_z axial velocity (cm s^{-1})
W gain or loss of energy (Einstein cm^{-3} sr^{-1} s^{-1})
X conversion (dimensionless)
x, y, z rectangular Cartesian coordinates (cm)
$\underline{x}$ spatial position vector (cm)
z axial coordinate (cm)

Greek letters

α_i kinetic parameter
β volumetric extinction coefficient (cm^{-1})
Γ global reflection coefficient (dimensionless)
ε_L liquid hold-up (dimensionless)
η directional cosine (dimensionless)
θ spherical coordinate (rad)
θ_n angle between the ray trajectory and the outwardly directed normal (rad)
κ volumetric absorption coefficient (cm^{-1})
λ radiation wavelength (nm)
μ directional cosine (dimensionless)

ν stoichiometric coefficient (dimensionless)
σ volumetric scattering coefficient (cm^{-1})
ϕ spherical coordinate (rad)
Φ primary quantum yield (mol $Einstein^{-1}$)
χ internal/external radius ratio (dimensionless)
Ω solid angle (sr)
$\underline{\Omega}$ unit vector in the direction of radiation propagation (dimensionless)

Subscripts

a air property
c relative to critical angle
exp experimental
F relative to formic acid
f relative to film
g relative to glass
HQ relative to hydroquinone
i relative to species i
L relative to the lamp
mod model
P relative to hydrogen peroxide
PCE relative to perchloroethylene
R reactor property
T total value
Tk tank property
W wall
λ dependence on wavelength
$\underline{\Omega}$ relative to the direction of propagation
0 relative to the reactor window at $x = 0$; also initial condition
4-CC relative to 4-chlorocatechol
4-CP relative to 4-chlorophenol

Superscripts

abs absorption
em emission
in inlet condition
in-scatt in-scattering
ou outlet condition
ou-scatt out-scattering

Special symbol

$^{\circ}$ initial condition
$\langle . \rangle$ average value
$\overline{(.)}$ averaged value over the wavelength interval

REFERENCES

Alfano, O.M., Cabrera, M.I., and Cassano, A.E. "Photocatalytic reactions involving hydroxyl radical attack. I. Reaction kinetics formulation with explicit photon absorption effects". *J. Catal.* **172**, 370 (1997).

Alfano, O.M., and Cassano, A.E. "Photoreactor modeling. Applications to advanced oxidation processes". *Int. J. Chem. React. Eng.* **6**(P2), 1 (2008).

Alfano, O.M., Negro, A.C., Cabrera, M.I., and Cassano, A.E. "Scattering effects produced by inert particles in photochemical reactors. 1. Model and experimental verification". *Ind. Eng. Chem. Res.* **34** (2), 488 (1995).

Alfano, O.M., Romero, R.L., and Cassano, A.E. "A cylindrical photoreactor irradiated from the bottom. III. Measurement of absolute values of the local volumetric rate of energy absorption. Experiments with polychromatic radiation". *Chem. Eng. Sci.* **41**, 1163 (1986).

Almquist, C.B., and Biswas, P.A. "A mechanistic approach to modeling the effect of dissolved oxygen in photo-oxidation reactions on titanium dioxide in aqueous systems". *Chem. Eng. Sci.* **56**, 3421 (2001).

Blelski, B.H.J., Cabe III, D.E., Arudi, R.L., and Ross, A.B. "Reactivity of HO_2/O_2^- radicals in aqueous solutions". *J. Phys. Chem. Ref. Data.* **4**, 1041 (1985).

Brandi, R.J., Alfano, O.M., and Cassano, A.E. "Modeling of radiation absorption in a flat plate photocatalytic reactor". *Chem. Eng. Sci.* **51**, 3169 (1996).

Brandi, R.J., Alfano, O.M., and Cassano, A.E. "Rigorous model and experimental verification of the radiation field in a flat plate solar collector simulator employed for photocatalytic reactions". *Chem. Eng. Sci.* **54**, 2817 (1999).

Brandi, R.J., Rintoul, G., Alfano, O.M., and Cassano, A.E. "Photocatalytic reactors. Reaction kinetics in a flat plate solar simulator". *Catal. Today* **76**, 161 (2002).

Buxton, G.V., Greenstock, C.L., Helman, W.P., and Ross, A.B. "Critical review of rate constants for reactions of hydrated electrons, hydrogen atoms and hydroxyl radicals ($\cdot OH/\cdot O^-$) in aqueous solutions". *J. Phys. Chem. Ref. Data* **17**, 513 (1988).

Cabrera, M.I., Negro, A.C., Alfano O.M., and Cassano, A.E. "Photocatalytic reactions involving hydroxyl radical attack. II. Kinetic of the decomposition of trichloroethylene using titanium dioxide". *J. Catal.* **172**, 380 (1997).

Cassano, A.E., and Alfano, O.M. "Reaction engineering of suspended solid heterogeneous photocatalytic reactors". *Catal. Today* **58**, 167 (2000).

Cassano, A.E., Martín, C.A., Brandi, R.J., and Alfano, O.M. "Photoreactor analysis and design: Fundamentals and applications". *Ind. Eng. Chem. Res.* **34**, 2155 (1995).

Dijkstra, M.F.J., Panneman, H.L., Winkelman, J.G.N., and Kelly, J.J. *Chem. Eng. Sci.* **57**, 4895 (2002).

Duderstadt, J.J., and Martin, W.R. "Transport Theory". Wiley, New York, (1979).

Imoberdorf, G.E., Irazoqui, H.A., Alfano, O.M., and Cassano, A.E. "Scaling-up from first principles of a photocatalytic reactor for air pollution remediation". *Chem. Eng. Sci.* **62**, 793 (2007).

Imoberdorf, G.E., Irazoqui, H.A., Cassano, A.E., and Alfano, O.M. "Modeling of a multi-annular photocatalytic reactor for PCE degradation in air". *AIChE J.* **52**, 1814 (2006).

Imoberdorf, G.E., Irazoqui, H.A., Cassano, A.E., and Alfano, O.M. "Photocatalytic degradation of tetrachloroethylene in gas phase on TiO_2 films: A kinetic study". *Ind. Eng. Chem. Res.* **44**, 6075 (2005).

Irazoqui, H.A., Cerdá, J., and Cassano, A.E. "The radiation field for the point and line source approximations and the three-dimensional source models. Applications to photoreactions".*Chem. Eng. J.* **11**, 27 (1976).

Labas, M.D., Zalazar, C.S., Brandi, R.J., Martín, C.A., and Cassano, A.E. "Scaling-up of a photoreactor for formic acid degradation employing hydrogen peroxide and UV radiation". *Helv. Chim. Acta* **85**, 82 (2002).

Mills, A., and Morris, S. "Photomineralization of 4-chlorophenol sensitized by titanium dioxide: A study of the initial kinetics of carbon dioxide photogeneration". *J. Photochem. Photobiol. A*. **71**, 75 (1993).

Mills, A., Morris, S., and Davies, R. "Photomineralisation of 4-chlorophenol sensitised by titanium dioxide: A study of the intermediates". *J. Photochem. Photobiol. A*. **70**, 183 (1993).

Minero, C., Catozzo, F., and Pelizzetti, E., "Role of adsorption in photocatalyzed reactions of organic molecules in aqueous TiO_2 suspensions". *Langmuir*. **8**, 481 (1992).

Ozisik, M.N. "Radiative Transfer and Interactions with Conduction and Convection". Wiley, New York (1973).

Palmisano, G., Addamo, M., Augugliaro, V., Caronna, T., Di Paola, A., García López, E., Loddo, V., Marcí, G., Palmisano, L., and Schiavello, M. "Selectivity of hydroxyl radical in the partial oxidation of aromatic compounds in heterogeneous photocatalysis". *Catal. Today*, **122**, 118 (2007).

Salaices, M., Serrano, B., and de Lasa, H.I. "Photocatalytic conversion of phenolic compounds in slurry reactors". *Chem. Eng. Sci*. **59**, 3 (2004).

Satuf, M.L., Brandi, R.J., Cassano, A.E., and Alfano O.M. "Experimental method to evaluate the optical properties of aqueous titanium dioxide suspensions". *Ind. Eng. Chem. Res*. **44** (17), 6643 (2005).

Satuf, M.L., Brandi, R.J., Cassano, A.E., and Alfano O.M. "Photocatalytic degradation of 4-chlorophenol: A kinetic study". *Appl. Catal. B: Environ.* **82**, 37 (2008).

Satuf, M.L., Brandi, R.J., Cassano, A.E., and Alfano O.M. "Quantum efficiencies of 4-chlorophenol photocatalytic degradation and mineralization in a well-mixed slurry reactor". *Ind. Eng. Chem. Res*. **46**(1), 43 (2007a).

Satuf, M.L., Brandi, R.J., Cassano, A.E., and Alfano O.M., "Scaling-up of slurry reactors for the photocatalytic degradation of 4-chlorophenol". *Catal. Today*, **129**, 110 (2007b).

Siegel, R., and Howell, J.R., "Thermal Radiation Heat Transfer". 4th edition. Hemisphere Publishing Corp., Bristol, PA, 2002.

Stefan, M.I., and Bolton, J.R. "Mechanism of the degradation of 1,4-dioxane in dilute aqueous solution using the UV/hydrogen peroxide process". *Environ. Sci. Technol*. **32**, 1588 (1998).

Terzian, R., Serpone, N., Minero, C., Pelizzetti, E., and Hidaka, H., *J. Photochem. Photobiol. A*. **55**, 243 (1990).

Theurich, J., Linder, M., and Bahnemann, D.W. "Photocatalytic degradation of 4-chlorophenol in aerated aqueous titanium dioxide suspensions: A kinetic and mechanistic study". *Langmuir*, **12**, 6368 (1996).

Turchi, C.S., and Ollis, D.F., "Photocatalytic degradation of organic water contaminants: Mechanisms involving hydroxyl radical attack". *J. Catal.* **122**, 178 (1990).

Yamazaki, S., and Araki, K., "Photocatalytic degradation of tri- and tetrachloroethylene on porous TiO_2 pellets". *Electrochemistry*, **70**, 412 (2002).

Zalazar, C.S., Labas, M.D., Martín, C.A., Brandi, R.J., Alfano, O.M., and Cassano, A.E. "The extended use of actinometry in the interpretation of photochemical reaction engineering data". *Chem. Eng. J.* **109**, 67 (2005).